Remote Sensing of Environment 238 (2020) 110929

Contents lists available at ScienceDirect

Remote Sensing of Environment

journal homepage: www.elsevier.com/locate/rse

Continuous subpixel monitoring of urban impervious surface using Landsat time series

Chengbin Deng[a,*], Zhe Zhu[b]

[a] Department of Geography, State University of New York at Binghamton, PO Box 6000, Binghamton, NY 13902, United States
[b] Department of Geosciences, Texas Tech University, Lubbock, TX 79409, United States

ARTICLE INFO

Keywords:
Landsat
Urban
Time series
Urban impervious surface dynamics
Continuous subpixel monitoring

ABSTRACT

A novel method called Continuous Subpixel Monitoring (CSM) was developed to map and monitor urban impervious surface change continuously at the subpixel level. Time series model of each pixel was first estimated based on clear Landsat observations between 2000 and 2014, and any land surface change was detected by the Continuous Change Detection and Classification (CCDC) algorithm. These coefficients and Root Mean Square Errors (RMSEs) of the estimated time series models were then employed as the inputs of random forest regressor. A few experiments with different combinations of variables and bands were explored to better construct random forest regression models. We successfully applied this algorithm to map subpixel urban impervious surface area (ISA%) and characterize its dynamics in Broome County, New York. Several conclusions can be drawn from the results and analyses. First, the integration of subpixel mapping technique and time series analysis in CSM can yield a relatively satisfactory ISA% result at one point in time. With higher precision and smaller bias, its mapping accuracy is better than that of National Land Cover Database (NLCD) percent developed imperviousness product, without using extensive auxiliary data, such as nighttime light image and transportation network. Second, the ISA% change of any time interval can be easily derived and detected by CSM with relatively high accuracy, which have the potential to generate sub-annual ISA% change products. Furthermore, this approach can detect not only urban expansion/intensification (ISA% gain), but also different patterns of urban transitions overtime, such as urban demolition/redevelopment to vegetation (ISA% loss), and surface modifications (no mechanical change). Finally, CSM works well in one of the cloudiest regions in the United States. This algorithm could provide a new direction to map and monitor percent urban impervious surface change in a reliable and efficient way, which also has the potential to apply to other land cover types (e.g., tree, shrub, and barren lands) at the subpixel level.

1. Introduction

Persisting dynamic urban changes have been taking place at an unprecedented level since entering the 21st century. Cohen (2004) and Seto (2009) summarized three urbanization characteristics in the past two decades. The first is the magnitude of urbanization. As a direct reflection of urbanization, approximately 55% of the world's population is now living in urban areas. Over 400 cities have a population size higher than 1 million, and 71 of them have more than 5 million inhabitants (United Nations Department of Economic and Social Affairs; UNDESA, 2018). Comparatively, only 16 cities had populations of 1 million or more in 1900. The second is the rapidity of urbanization, which takes less time to increase the percentage of the global population living in urban areas. Between 1800 and 1900, populations residing in urban areas increased from 3% of the world's population to 14%. Only after 50 years in 1950, the percentage doubled and reached approximately 30%. This number is projected to reach 66% by 2050 (United Nations, 2015). The third characteristic is the concentration of urbanization with future population increase primarily in Africa and Asia, especially India, China, and Nigeria. Growing population needs sufficient food, water, and living space. As a consequence, natural lands are transformed continuously into farmlands and urban lands. Although urban areas only account for 3% of the Earth's surface (Potere and Schneider, 2007), the urbanization process results in a series of human-induced environmental issues. For example, the increase of impervious surfaces remarkably degrades stream hydrology and ecosystem functions, including riverine physical alternation, hydrological changes (e.g., increasing runoff volume and peak flow, and accordingly, urban

* Corresponding author.
E-mail address: cdeng@binghamton.edu (C. Deng).

https://doi.org/10.1016/j.rse.2018.10.011
Received 22 February 2018; Received in revised form 1 October 2018; Accepted 6 October 2018
Available online 19 October 2018

flooding), and degradation of water quality (Arnold and Gibbons, 1996; Brabec et al., 2002; Center for Watershed Protection, 2003; Chabaeva et al., 2009; Meyer et al., 2005; Paul and Meyer, 2001; Schueler, 1994; Schueler et al., 2009; Skougaard Kaspersen et al., 2017). Also, the growing urban impervious surfaces result in the increase of air temperature as well as urban heat island phenomenon (Deng and Wu, 2013a; Weng et al., 2004; Yuan and Bauer, 2007). Moreover, as pointed out in a recent United Nations report (2015), in addition to the trend of increasing urban populations, declining populations in specific areas should also be noticed, due mainly to economic contraction, low fertility rate, and natural disasters. Distinct urban transitions can be notably found in cities that are experiencing different migration status and economic transformations. To better understand the impacts of urban transformations in various cities, the very first task is to record, monitor and analyze a complete evolution process of a city.

To accurately detect urban change and characterize urban dynamics, we need to better consider the spatial and temporal requirements. In the spatial domain, due to the nature of heterogeneity in urban environments, more spatial details are preferable. The amount of land available for living, business, transportation, and leisure is very limited in urban areas, especially when the needs of human beings are increasing dramatically. Different land uses and land covers are intertwined, and a variety of manmade materials are used for construction. Mixed pixel issue is severe on satellite imagery of any urbanized areas. Despite the availability of some high-resolution satellite data, they are only appropriate to derive land surface information at a specific time, and do not have a long monitoring history like Landsat which dates back to 1970s. To take advantage of the longest continuous satellite records with Landsat, one potential solution is subpixel mapping. Mapping land covers at the subpixel level are generally derived by spectral unmixing (Adams et al., 1986; Deng and Wu, 2013; Nash and Conel, 1974; Powell et al., 2007; Roberts et al., 1998), or machine learning methods (Coulston et al., 2013; Coulston et al., 2012; Deng et al., 2017; Deng and Wu, 2013c; Xian et al., 2015; Xian et al., 2013; Yang et al., 2003a). Despite the effectiveness of the proposed subpixel mapping approaches in these pilot studies, fractional land covers using these methods are usually obtained at one point or a few points in time (Gao et al., 2012; Li et al., 2016; Michishita et al., 2012; Shahtahmassebi et al., 2016; Xiam et al., 2011; Xian and Homer, 2010), which is insufficient for documenting the complete process of urban transitions. For example, the widely used National Land Cover Dataset (NLCD) of the Conterminous United States (CONUS) usually update every five years (Xiam et al., 2011; Xian and Homer, 2010), and any change within the five year period is unknown. Another limitation of most subpixel mapping approaches is that the estimated land cover fractions from different time points are generally not recommended for change detection, due to the likelihood of including compounded errors from subpixel mapping (Zhu, 2017). Furthermore, a recent study shows that atmospheric correction, seasonality, environment settings, and the use of multi-temporal images also affect the accuracy of subpixel mapping (Deng et al., 2017).

In the temporal domain, dense satellite time series has become more and more popular for detecting land cover change. For moderate spatial resolution satellites like Landsat, change detection algorithms are shifting from decadal (Homer et al., 2015; Masek et al., 2008) and annual scales (Cohen et al., 2010; Hansen et al., 2000; Huang et al., 2010) to sub-annual scales (Brooks et al., 2014; Hamunyela et al., 2016; Hansen et al., 2016; Zhu and Woodcock, 2014a). Compared to other sub-annual scale algorithms that are mainly used to detect forest change, the Continuous Change Detection and Classification (CCDC; Zhu et al., 2015a; Zhu and Woodcock, 2014a) is capable of monitoring a variety of land cover and land use change continuously based on newly collected Landsat images. However, CCDC and other sub-annual scale change detection algorithms can only provide categorical change results (change or stable), which may not be appropriate for mapping heterogeneous urban environments, as the aforementioned mixed pixel issue severely affects the mapping accuracy of urban impervious surface.

Although success has been respectively achieved in spatial and temporal domains, the summarized paradox review has not been fully solved in the literature: subpixel mapping can provide more spatial details, but it fails to provide temporal change information, while most of the change detection studies fail to consider the mixed pixel issue in the urban area when using a dense stack of Landsat time series. Therefore, the general objectives of this research are to better address the paradox at two scales and to achieve the goal of continuous mapping. A method called Continuous Subpixel Monitoring (CSM) is proposed in this research, which integrates subpixel mapping techniques and time series analysis. Specifically, this algorithm aims to improve the mapping accuracy of urban impervious surface at the subpixel level, and to detect urban transitions by continuously monitoring with Landsat time series. It is worth noting that the use of "continuous" in its term implies that this method is both spatially and temporally continuous. In the spatial domain, continuous field of urban impervious cover (0 to 100%) is estimated for subpixel mapping. In the temporal domain, it consistently monitors urban land surface with Landsat time series and allows the most recent image to be added in the model for continuous monitoring overtime.

2. Study area and data

Located in Southern Tier of upstate New York and close to the Pennsylvania border, Broome County in New York State in the United States was used as the study area of this research (See Fig. 1). The area size of Broome County is 1854 km^2. The population of this study area is 200,600 according to 2010 Census, and it is decreased to193,639 (a drop of 3.5%) in 2017 based on the most recent population estimates of American Community Survey (United States Census Bureau, 2017). Primary human settlements in Broome County include the City of Binghamton (which is also the county seat) and its neighboring villages, Johnson City, and Endicott. These cities and villages are also known as Triple Cities Area. Scattered settlements can be found in the surrounding suburban and rural areas outside Triple Cities Area. Typical land covers in temperate regions appear in Broome County, including low to high density developed lands, forests (dominated by deciduous forests), barren lands, wetlands, pasture, and cultivated lands. According to the historical Census statistics (United States Census Bureau, 1995; 2001; 2017), Broome County has been experiencing a persistent population loss since the 1970s. Therefore, this area can serve as an example of shrinking cities in the Rust Belt in Northeastern and Midwest United States. Different from cities at the urbanization stage (such as those in the Sun Belt region in the U.S. and Southeast coast in China), urban lands in post-industrial cities can be revered to convert back into vacant lands on which grass and trees will regrow (Deng and Ma, 2015). Examples include the demolitions of blighted properties or brownfields, and the demolitions of building structures that are damaged by flood, fire, and collapse. The urban transition patterns of such post-industrial shrinking cities have rarely been studied. Besides, we have sufficient and abundant local knowledge. Specifically, we have a number of local resources to obtain and validate samples, such as colleagues who have been living in this area for all their lives and know this area very well, as well as local field visit to the locations. In addition, a notable challenge in our study area is the heavy cloud coverage. Binghamton is one of the top 10 cloudiest cities in the CONUS. Based on the statistics of comparative climatic observation data from National Oceanic and Atmospheric Administration (NOAA) over the past 44 years, on average 314 days in a year are cloudy or partially cloudy for this region (NOAA, 2015). The severe cloud coverage substantially affects the Landsat image quality for mapping subpixel urban impervious surface, and as a result, most of Landsat images in our study area are contaminated by cloud and cloud free images can hardly be found.

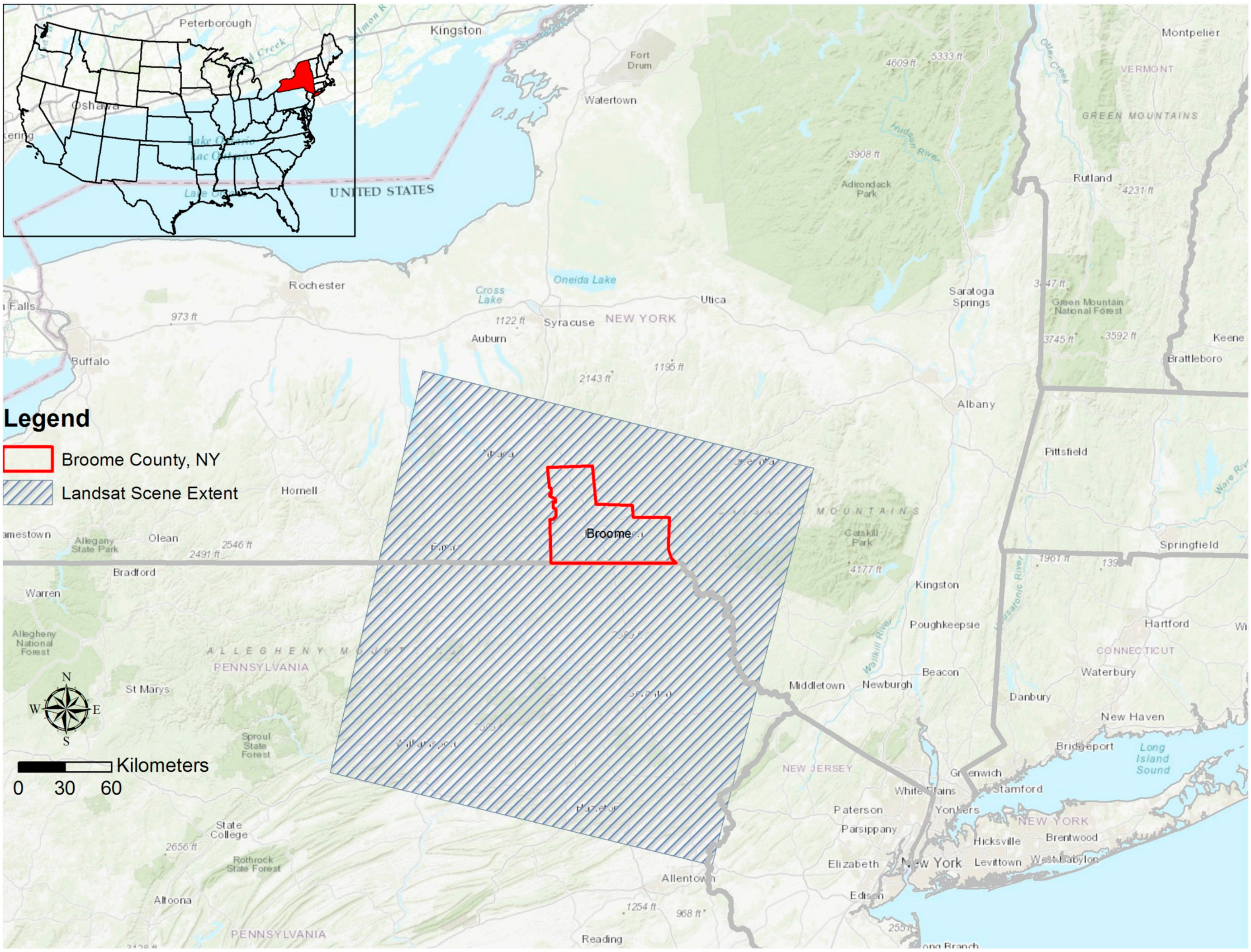

Fig. 1. Study area: Broome County (the red polygon), New York, United States. (For interpretation of the references to color in this figure legend, the reader is referred to the web version of this article.)

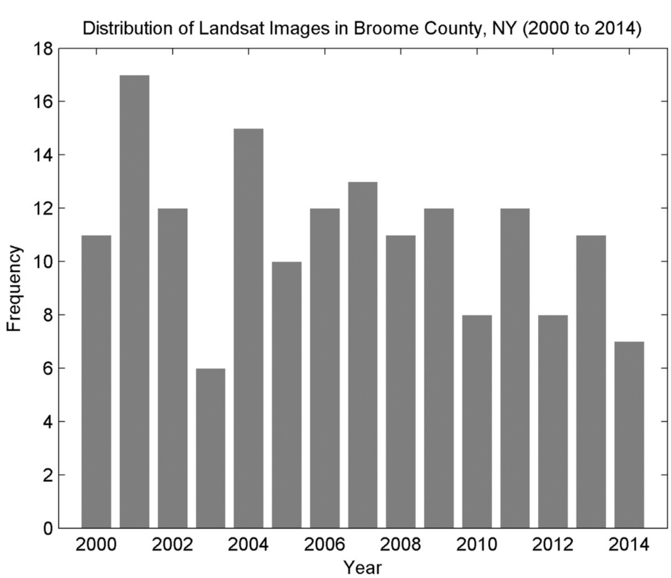

Fig. 2. Temporal distribution of involved Landsat images.

All Landsat images with relatively small cloud coverage (less than 20% of the entire scene) taken between 2000 and 2014 were collected. To derive land surface reflectance images for three different Landsat satellites, atmospheric correction was implemented using different tools. The Landsat Ecosystem Disturbance Adaptive Processing System (LEDAPS) (Schmidt et al., 2013) was used for all Landsat 5 TM and 7 ETM+ images, while the Landsat 8 Surface Reflectance (L8SR) system (Vermote et al., 2016) was processed for all Landsat 8 OLI images. Overall, 165 Landsat images were downloaded from and preprocessed by the U.S. Geological Survey (USGS) website, and their annual distribution is displayed in Fig. 2. The shapefile of Broome County was downloaded from the website of U.S. Census Bureau, by which the portion containing the study area was subdivided from all Landsat images. For comparison purposes, the historical 2006 and 2011 NLCD products of land cover classification, percent imperviousness and the percent change from 2006 to 2011 were all collected, and partitioned to the extent of Broome County. 2011 NLCD products are the most recent land cover products created by USGS. With a long history which dates back to 1992 as well as a large geographic coverage of CONUS, this product has been widely used for a variety of applications by different federal agencies, such as U.S. Forest Services, U.S. Department of Agriculture, Environment Protection Agency, and name a few. Orthophotographs taken in 2006, 2011 and 2014 were also downloaded from the website of National Agriculture Imagery Program (NAIP). Reference

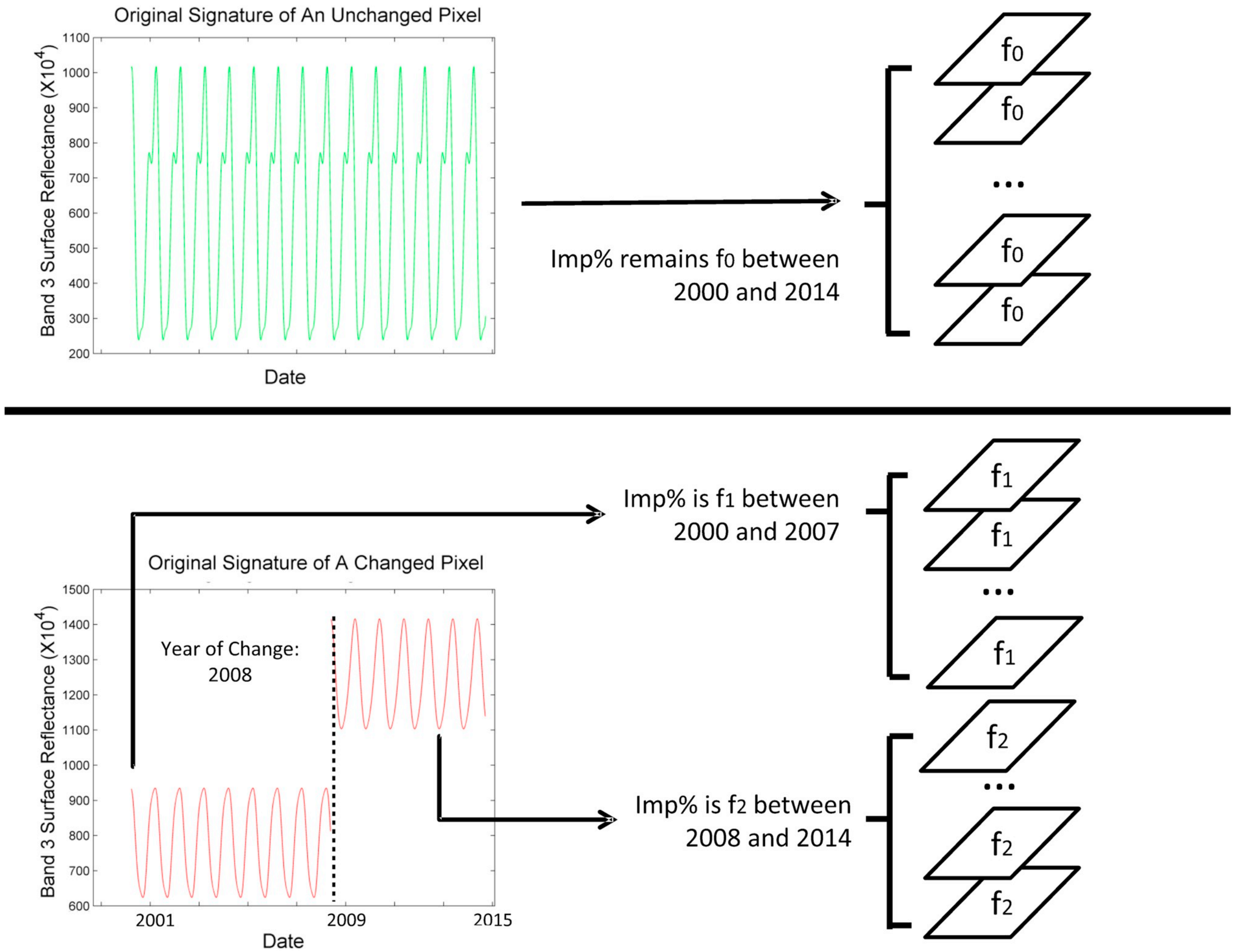

Fig. 3. Processing of stable and changed pixels using CSM, in which time series models are shown using Landsat Band 3. Upper panel illustrates a stable pixel of which impervious surface fraction remains f_0; lower panel shows a changed pixel of which impervious surface fraction changes from f_1 (between 2000 and 2007) to f_2 (between 2008 and 2014).

information was derived by manual interpretation and digitizing on these aerial photographs. All datasets were re-projected to Universal Transverse Mercator (UTM) projection (Zone 18 North) with a WGS84 datum.

3. Methodology

The proposed CSM algorithm consists of two major steps: (1) time series model estimation and continuous change detection, and (2) fractional land cover estimation. In this study, we used this method to map subpixel urban impervious surface and its dynamics.

3.1. Time series model estimation and continuous change detection (CCD)

To acquire time series of clear-sky observations, cloud, cloud shadow, and snow (unless it is perennial snow) are screened based on Function of mask (Fmask) (Zhu et al., 2015a; Zhu and Woodcock, 2012) and multiTemporal mask (Tmask) algorithms (Zhu and Woodcock, 2014b). The clear-sky observations are then estimated based on three sets of Fourier series models: simple, advanced, and full models (Eqs. 1–3) (Zhu et al., 2015b). The more complex the time series model, the better performance in modeling intra-annual differences in the time series data will be. The simple model needs at least 12 clear-sky observations, while between 18 and 24 clear-sky observations will invoke the advanced model, and more than 24 observations initialize the full model. The time series coefficients are estimated based on the Least Absolute Shrinkage and Selection Operator (LASSO) regression (Friedman et al., 2008; 2010), with a fixed value of lambda (20). The LASSO regression minimizes the residual sum of squared errors with a bound on the sum of the absolute values of the coefficients, which provides accurate model estimation without overfitting (Zhu et al., 2015a).

$$\hat{\rho}\,(i,x)_{simple} = a_{0,i} + a_{1,i}\cos\left(\frac{2\pi}{T}x\right) + b_{1,i}\sin\left(\frac{2\pi}{T}x\right) + c_{1,i} \qquad (1)$$

where,

x: Julian date

i: The ith Landsat Band (i = 1, 2, 3, 4, 5, and 7)

T: Number of days per year (T = 365)

$a_{0,\ i}$: Coefficient for overall value for the ith Landsat Band when x is 0

$a_{1,\ i}$, $b_{1,\ i}$: Coefficients for intra-annual change for the ith Landsat Band

$c_{1,\ i}$: Coefficient for inter-annual change (slope) for the ith Landsat Band

$\hat{\rho}\,(i,x)_{simple}$: Surface reflectance for the ith Landsat Band at x Julian date from simple model.

$$\hat{\rho}\,(i,x)_{advanced} = \hat{\rho}\,(\mathrm{i},x)_{simple} + a_{2,i}\cos\left(\frac{4\pi}{T}x\right) + b_{2,i}\sin\left(\frac{4\pi}{T}x\right) \qquad (2)$$

Where,

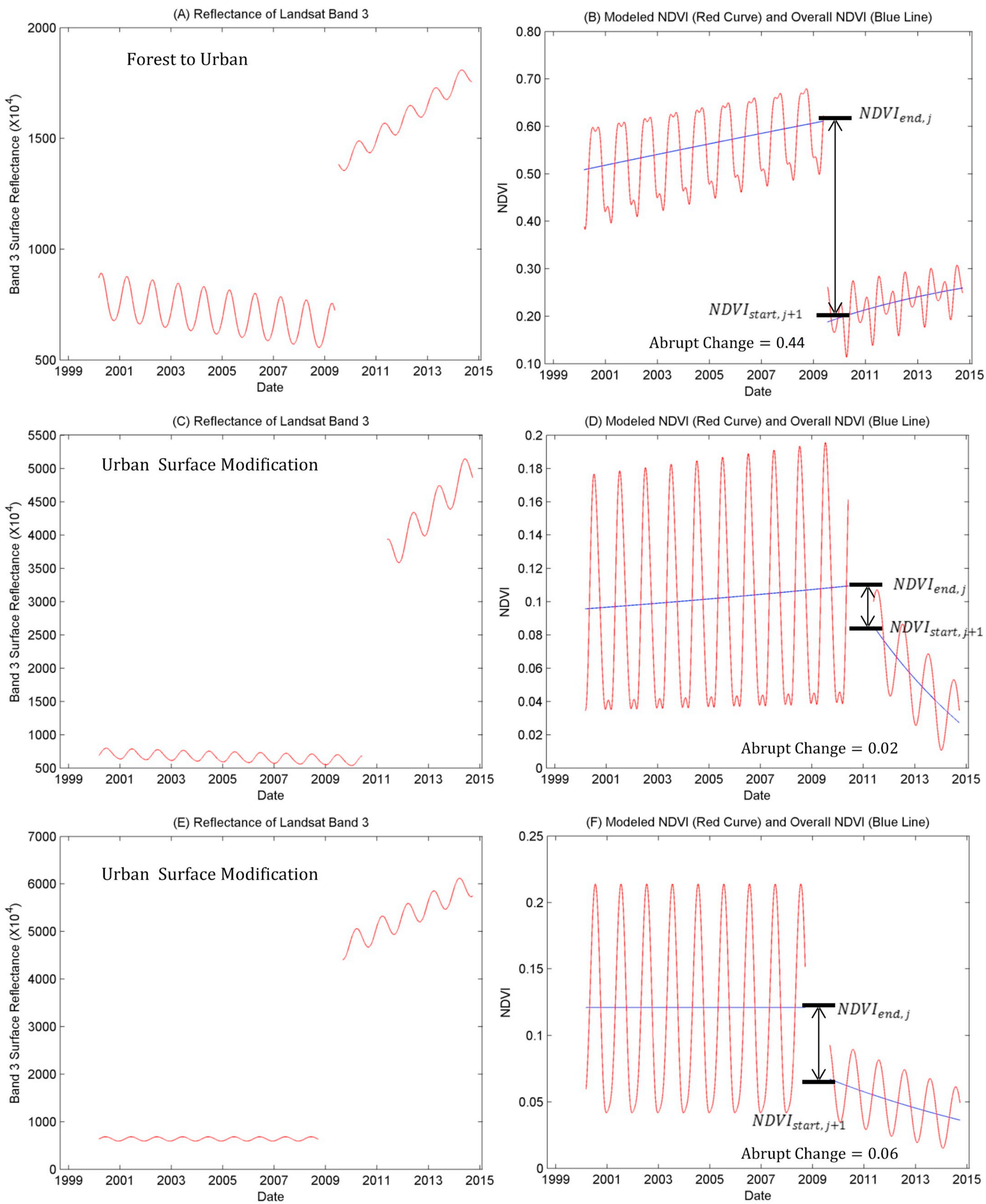

Fig. 4. The changes of Band 3 reflectance (first column) and NDVI (second column) of three examples. The red curve shows the modeled NDVI that characterizes seasonality, and the blue line is the overall NDVI that minimizes seasonality. The first row is a pixel from forest to urban. The second and third are two different pixels of surface modification with new painting. (For interpretation of the references to color in this figure legend, the reader is referred to the web version of this article.)

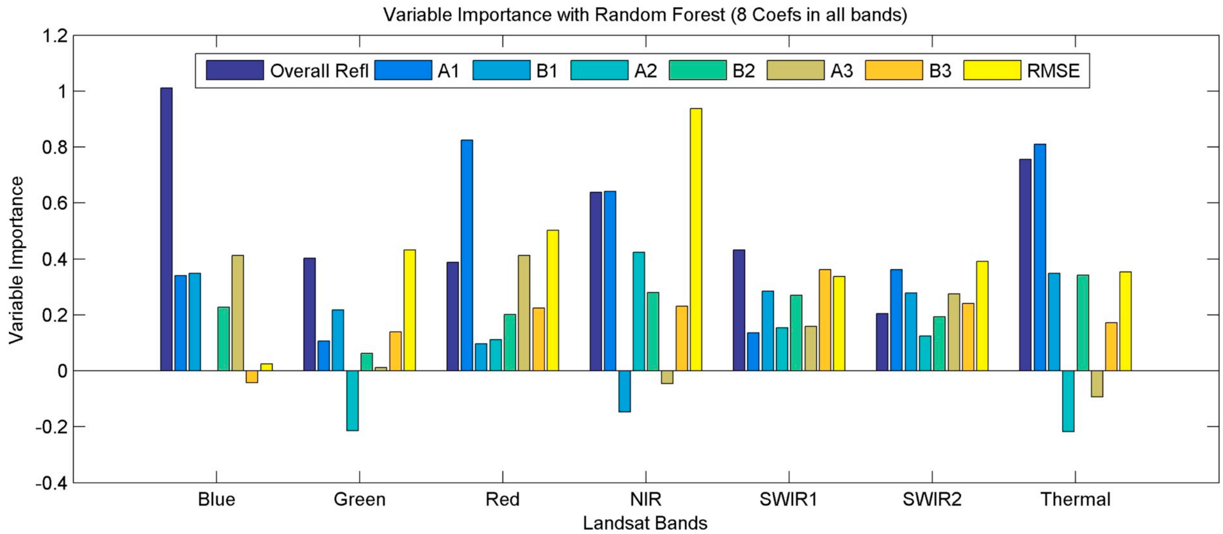

Fig. 5. Variable importance when using all the time series model coefficients of all optical and thermal bands as inputs in random forest. (For interpretation of the references to color, the reader is referred to the web version of this article.)

$a_{2,\ i}$, $b_{2,\ i}$: Coefficients for intra-annual bimodal change for the ith Landsat Band

$\hat{\rho}\,(i,x)_{advanced}$: Surface reflectance for the ith Landsat Band at x Julian date from advanced model.

$$\hat{\rho}\,(i,x)_{full} = \hat{\rho}\,(i,x)_{advanced} + a_{3,i}\cos\left(\frac{6\pi}{T}x\right) + b_{3,i}\sin\left(\frac{6\pi}{T}x\right) \tag{3}$$

where,

$a_{3,\ i}$, $b_{3,\ i}$: Coefficients for intra-annual trimodal change for the ith Landsat Band.

$\hat{\rho}\,(i,x)_{full}$: Surface reflectance for the ith Landsat Band at x Julian date from full model. By comparing predictions from the estimated time series model with actual observations, changes are detected if the difference is larger than a threshold *six* times consecutively. If no change is detected, new clear-sky observations will be added to the time series, and the model will be estimated again. To detect many kinds of surface change, all spectral bands except Blue and TIR bands are used to define a change, and the change threshold is derived by normalizing change vector magnitude with Root Mean Squared Errors (RMSEs) from the time series model fit for each spectral band.

3.2. Fractional land cover estimation

3.2.1. Training samples generation and variable selection for random forest

Random Forest was developed by Breiman (2001) for classification and prediction. This method now becomes one of the most effective machine learning approaches and is popularly used for remote sensing images per-pixel and subpixel classification. In this research, we derived 50 bagged regression trees at each decision split, of which the prediction results were taken into consideration for the final output of every estimate. A total of 600 random samples were initially obtained using a stratified random sampling strategy for training purposes. Among these samples, half of which were in Triple Cities Area and the other half was in suburban and rural areas of Broome County. The configuration of these random samples was matched perfectly with that of the Landsat pixels. The urban impervious surfaces within each Landsat pixel sample were then manually digitized on the 2014 high-resolution NAIP aerial photograph. All digitized urban impervious surface areas within the same individual pixel were summed. Percent urban impervious surface was then calculated as the total sum of all urban impervious surface divided by the size of a Landsat pixel (i.e., 900 square meters). The input variables of random forest model are the time series model coefficients and RMSEs of all bands from the model fit. For each spectral band, there are eight input variables, which include one variable represent the overall reflectance value at the center of the time series model by combining the constant (a0) and slope (c1) coefficients (see Zhu and Woodcock, 2014a for details), an RMSE as the indicator of model fit, and three pairs of (a total of six) coefficients to characterize the intra-annual change (Zhu et al., 2015b). Overall, there were 56 input variables from the seven Landsat bands (i.e., six optical bands and one thermal band). That said, only time series model coefficients and RMSEs are used as inputs of random forest, rather than using the actual surface reflectance at a certain time. These model coefficients reflect the overall spectral reflectance and periodic phenological features of any pixel on the image. However, using too many input variables in random forest may introduce noise in the model instead of useful land cover information (Zhu and Woodcock, 2012). To construct a better random forest model, our initial attempt was to use all 56 variables from the seven Landsat bands as the inputs in random forest. We calculated the variable importance, and then iteratively removed variables with the smallest value of importance. The random forest regressor with the best accuracy indicators was then selected to map the entire study area during fifteen years. It is worth noting that, due to the continuous nature of the time series models, the random forest model can be applied to the fractional impervious surface estimation of any pixel at any given time once the random forest model is trained with the samples from one point in time.

3.2.2. Estimation of fractional urban impervious surface for stable and changed pixels

Theoretically, fractional land cover at any time interval can be estimated in the result stack by using the trained random forest model. For illustration purposes, we generated an annual result stack of fractional urban impervious surface. A simple rule is designed to generate the annual stack by taking into consideration the status of land cover dynamics (see Fig. 3). For stable pixels, urban impervious surface fraction remained consistently unchanged throughout the study period of fifteen years, as shown in the upper panel of Fig. 3. For changed pixels, the time of change was identified first, and the fraction in each period was estimated, respectively. In each relative stable period, the impervious surface fraction should remain unchanged. The result at the year of change will be assigned with the fraction after the change, regardless of the change time in this year (for instance, even it is in December). The process for changed pixels is displayed in the lower panel of Fig. 3.

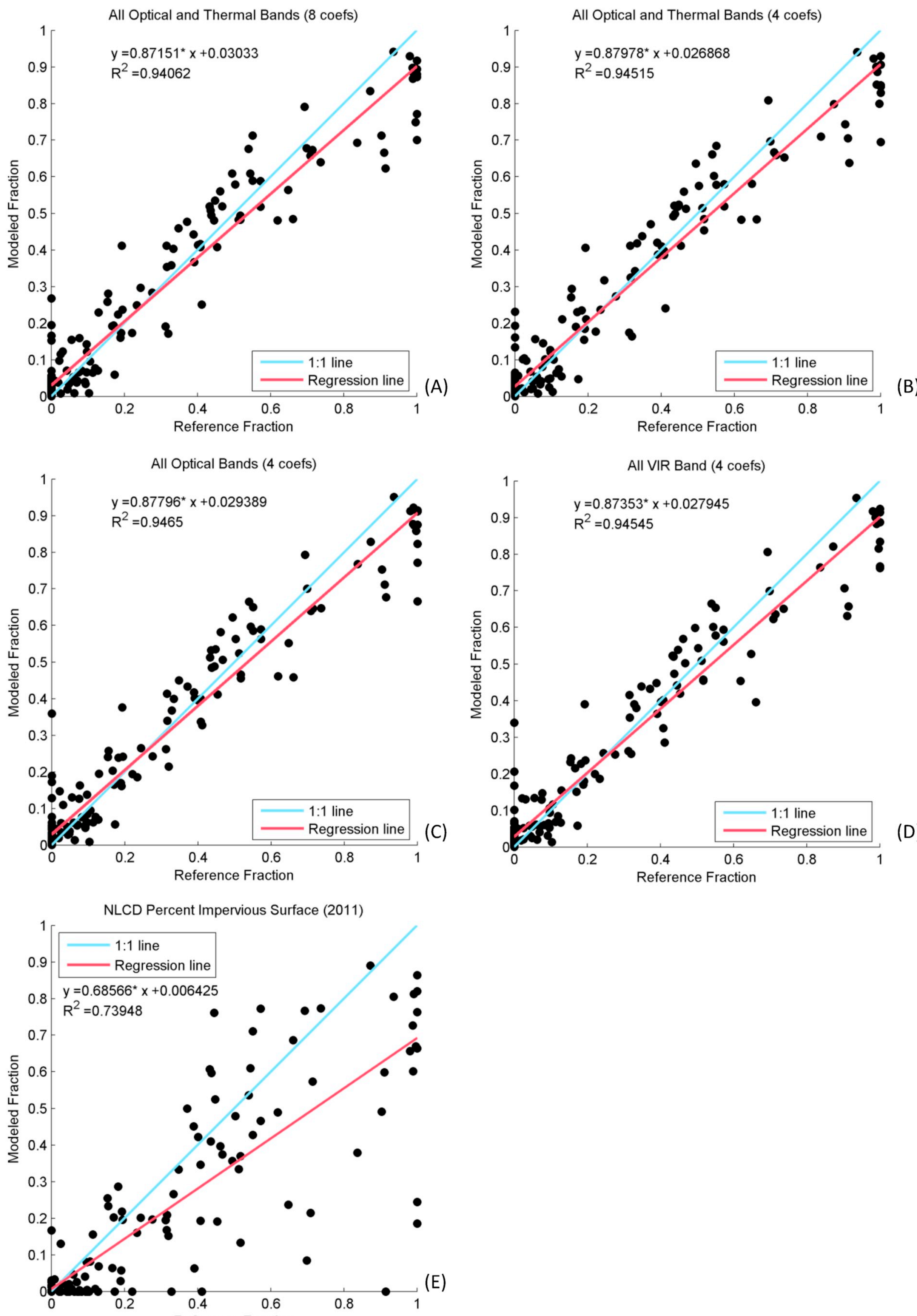

Fig. 6. Scatterplots of modeled impervious surface fraction in 2011 using (A) all eight variables (all model coefficients) per band with all bands, (B) only four variables (overall reflectance, a1, b1, and RMSE) per band with all bands, (C) the same four variables per band with all optical bands (all bands but excluding thermal band), and (D) the same four variables per band with only four VIR bands, and (E) from the 2011 NLCD product.

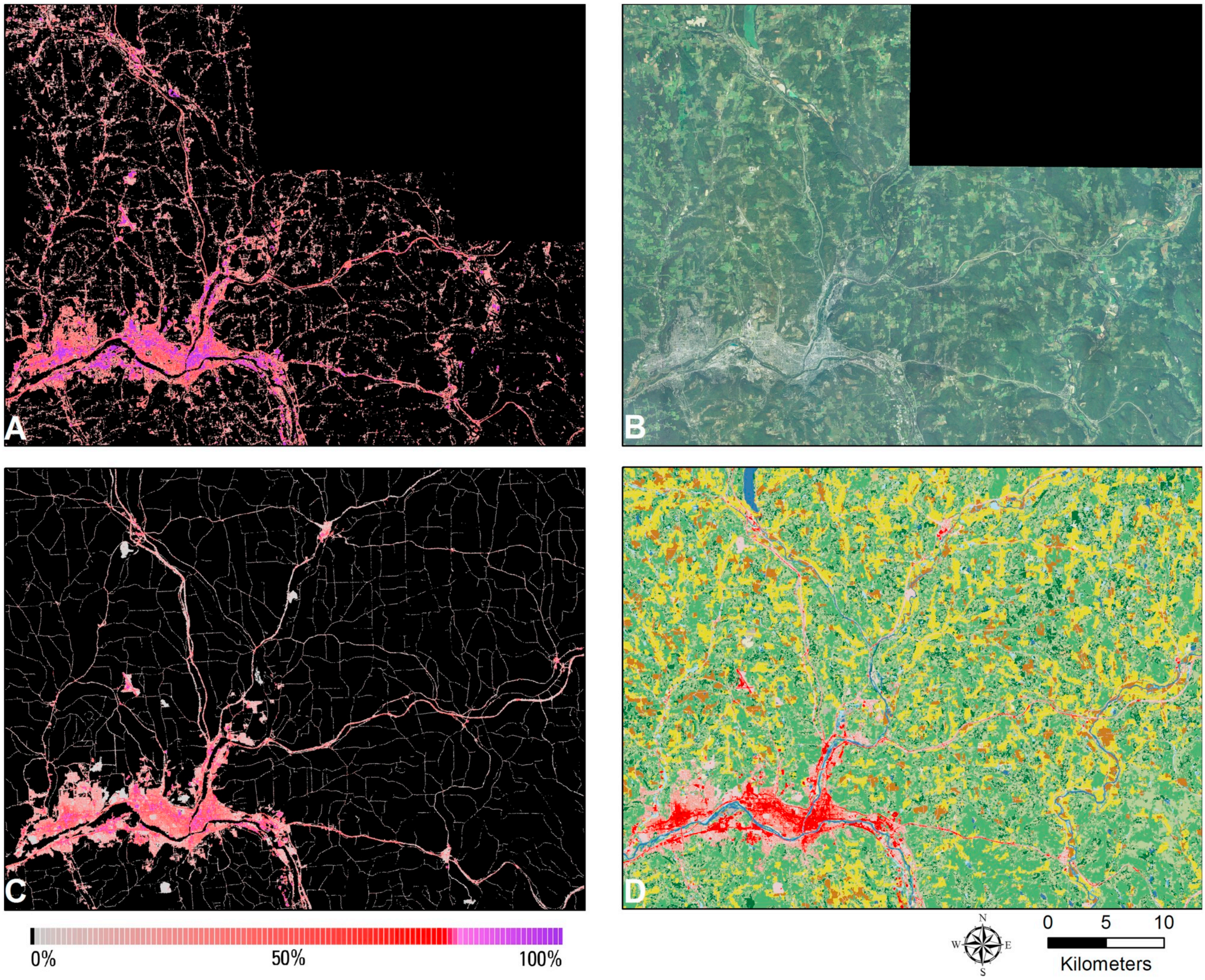

Fig. 7. (A) CSM-modeled result of impervious surface abundance in the entire Broome County in 2011, and comparisons with (B) 2011 NAIP aerial photograph, (C) 2011 NLCD percent developed imperviousness product, and (D) 2011 NLCD land cover classification product.

3.2.3. Removal of surface modification without mechanical changes

Surface modification is defined as any change on urban impervious surface but without mechanical change. That said, although urban surface has experienced a certain type of modification which can be detected in the first step of CCD, no impervious surface increase or decrease actually occurs. Surface modification, therefore, should not be considered as urban impervious surface change. Through visual examination, the examples of surface modification in our study area include tile replacement, new painting in parking lots, and new coating on the building roofs for maintenance purposes (such as waterproofing leak repair). According to our experiments, we found this type of pseudo "change" with a range from 5% to 20% overtime, depending on the number of surface modifications in an urban area. To remove surface modifications, we adapted the NDVI abrupt change index (Zhu et al., 2016). This indicator is calculated as the overall NDVI difference before and after the change, where overall NDVI characterizes the overall trend of NDVI which minimizes its seasonal impact (Zhu et al., 2016). This metric can be formalized as follows.

$$A_j = |NDVI_{start,j+1} - NDVI_{end,j}| \quad (4)$$

where Aj is the abrupt change index; $NDVI_{end,\ j}$ is the overall NDVI value at the ending point in stable period j before the change; $NDVI_{start,\ j+1}$ is the overall NDVI value at the starting point in stable period $j + 1$ after the change. Fig. 4 illustrates three examples in our study area with changes detected by CCDC (including one mechanical change from forest to urban, and two surface modifications), as well as their associated reflectance and NDVI overtime. It can be discerned that a high value of NDVI abrupt change is associated with a real mechanical change, and lower ones with surface modification. A sensitivity analysis was performed to obtain the optimal threshold, in which the producer's and user's accuracy of changed percent urban impervious surface were calculated following the literature (Wickham et al., 2013).

3.3. Accuracy assessment

To evaluate the performance of the proposed CSM algorithm, another set of 400 random samples was generated based on the stratified random sampling strategy. Half of these validation samples were randomly selected from the changed areas that are identified by CCD, while the other half was randomly selected from the non-changed area. These samples of fractional urban impervious surface were manually digitized on the 2006 and 2011 high-resolution aerial photographs, respectively. We used these independent testing samples to assess the accuracy of (1) the modeled fractional impervious surface at one point in time (in 2011), and (2) the resultant percent change accuracy between two timestamps (i.e., changes of subpixel impervious surface from 2006 to 2011 in accordance with the NLCD percent change product). Three widely used indicators were calculated for evaluating the

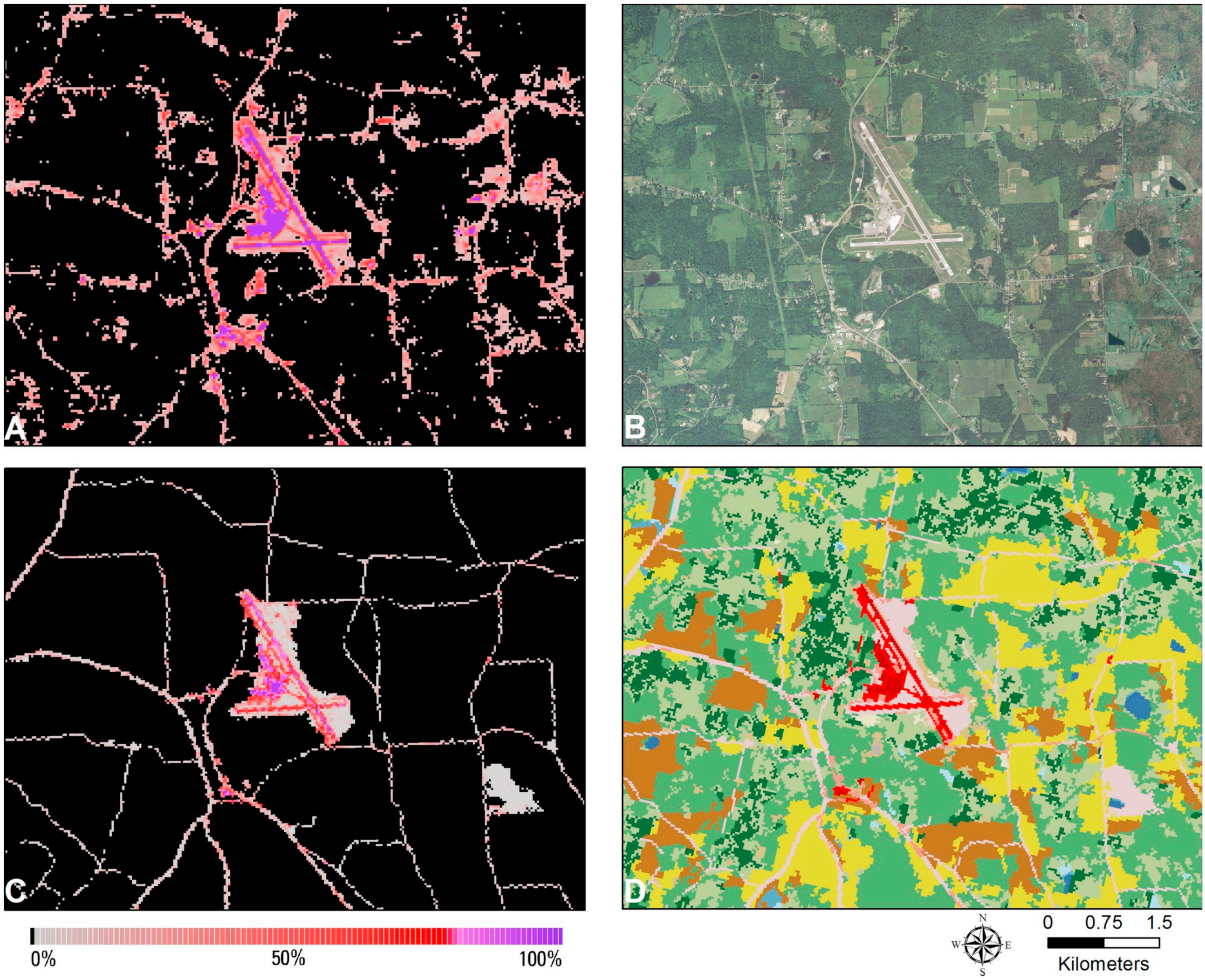

Fig. 8. (A) CSM-modeled subpixel urban impervious surface distribution in a rural area (near the Greater Binghamton Airport) in 2011, and comparisons with (B) 2011 NAIP aerial photographs, (C) 2011 NLCD percent developed imperviousness product, and (D) 2011 NLCD land cover classification products.

accuracy, including RMSE, Mean Absolute Error (MAE) and Systematic Error (SE). The first two are used to measure the precision, while the latter one is used to quantify estimation bias. They can be formulated as follows.

$$RMSE = \sqrt{\frac{1}{n}\sum_{i=1}^{n}(\widehat{f_i} - f_i)^2} \tag{6}$$

$$MAE = \frac{1}{n}\sum_{i=1}^{n}|\widehat{f_i} - f_i| \tag{7}$$

$$SE = \frac{1}{n}\sum_{i=1}^{n}(\widehat{f_i} - f_i) \tag{8}$$

where $\widehat{f_i}$ is the estimated subpixel urban impervious surface of sample i using random forest; f_i is the digitized fraction of urban impervious surface of sample i from the high-resolution aerial photographs; and n is the total number of sample polygons. To better evaluate the performance of the proposed algorithm, these metrics are also examined in areas with different urbanization level, i.e., low and high density developed areas using an impervious percentage of 30% as a cut-off point (Deng, 2016; Wu, 2004). In addition, scatterplots were drawn to validate the estimated urban impervious surface fraction both at one point in time and the percent change from 2006 to 2011. This is done by plotting the modeled fraction against the reference fraction by manual digitizing.

4. Results

4.1. Selection of input variables in random forest

A random forest model was built by using all 56 variables from time series model coefficients and model fits of all Landsat bands. The variable importance of this random forest model was displayed in Fig. 5 for further variable selections. We have observed several findings as follows. First, concerning specific input variables, overall reflectance at the center of the time series model (hereafter, we will call it overall reflectance for simplification) plays a vital role in this random forest model (shown as dark blue bars). This can be supported by its ranking in all bands (except for the SWIR2 Band), where overall reflectance consistently ranked as one of the top three variables with the highest importance. In addition to overall reflectance, RMSE (shown as the yellow bars) and phenological coefficients (i.e., a1 and b1; shown as blue and light blue, respectively) also have relatively high importance in this random forest regressor. Comparatively, the bimodal coefficients (i.e., a2 and b2) and trimodal coefficients (i.e., a3 and b3) are less important in the model. The importance values of these bimodal and trimodal coefficients (shown as green, light green, tan and orange bars,

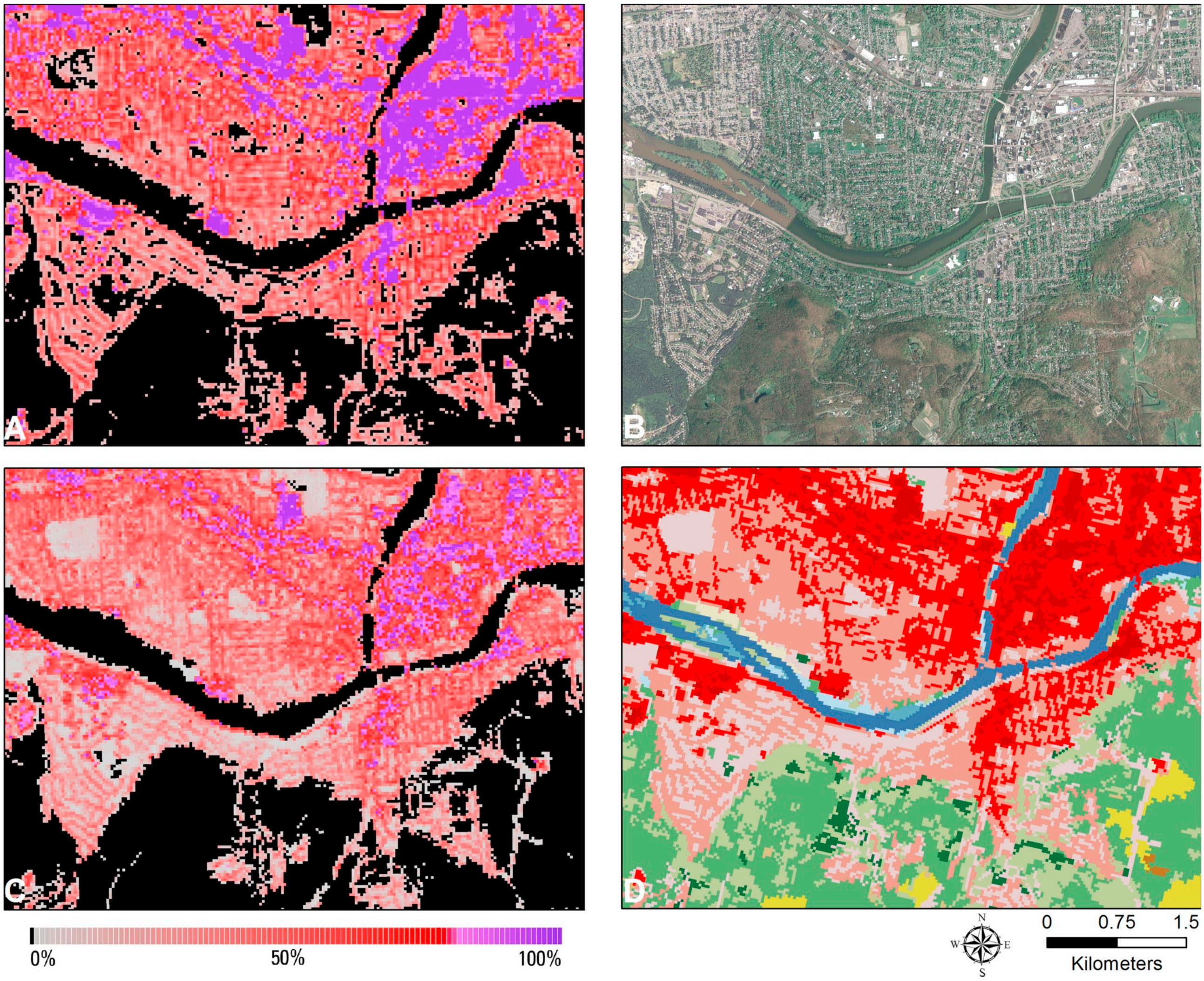

Fig. 9. (A) CSM-modeled subpixel urban impervious surface distribution in downtown Binghamton in 2011, and comparisons with (B) 2011 NAIP aerial photographs, (C) 2011 NLCD percent developed imperviousness product, and (D) 2011 NLCD land cover classification products.

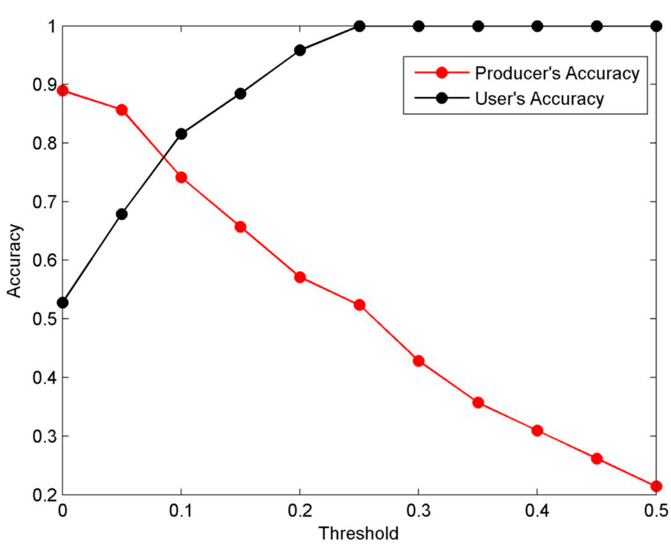

Fig. 10. Sensitivity analysis of changed percent urban impervious surface using different thresholds of NDVI abrupt change to exclude surface modification.

respectively) are much lower than other time series model coefficients, and some of them in certain bands even have a negative value. This may be explained by the fact that, unlike the phenological change of vegetation, the seasonality of urban impervious surface at higher frequencies (i.e., the bimodal and trimodal coefficients of time series models) is not very apparent, and it may be unnecessary to employ such a complicated time series model. Second, with respect to specific Landsat bands, four VIR bands (Blue, Green, Red, and NIR Bands) have higher variable importance than other bands. As shown in Fig. 5, each of the VIR bands has at least one variable with a relatively high importance. Comparatively, despite the important role of overall reflectance and a1, the thermal band has two input variables with negative values. This suggests that the performance of the thermal band is not very stable when using all coefficients of time series model. Also, the importance values of Landsat bands 5 and 7 (i.e., SWIR 1 and 2) seem not to be very high. It is, therefore, worth testing the model performance without specific input variables and bands, as the inclusion of them may introduce noise rather than useful information in the random forest model. Based on the derived variable importance, we performed three additional random forest models with different variable combinations and band combinations. These include the random forest model only with four variables (overall reflectance, a1, b1, and RMSE) in all bands, model with the same four variables in all optical

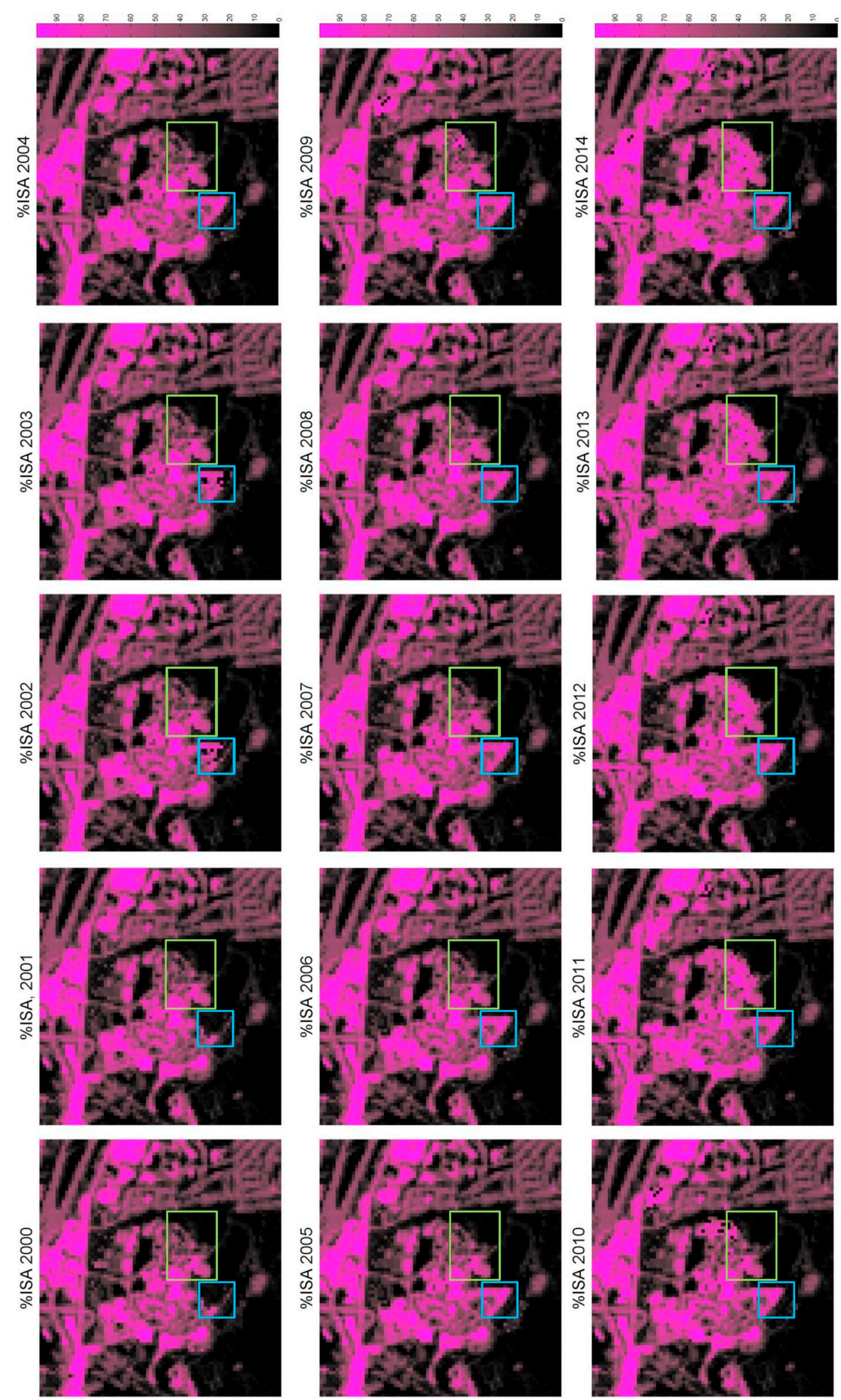

Fig. 11. CSM-modeled annual percent urban impervious surface increase on the campus of SUNY-Binghamton between 2000 and 2014. (For interpretation of the references to color, the reader is referred to the web version of this article.)

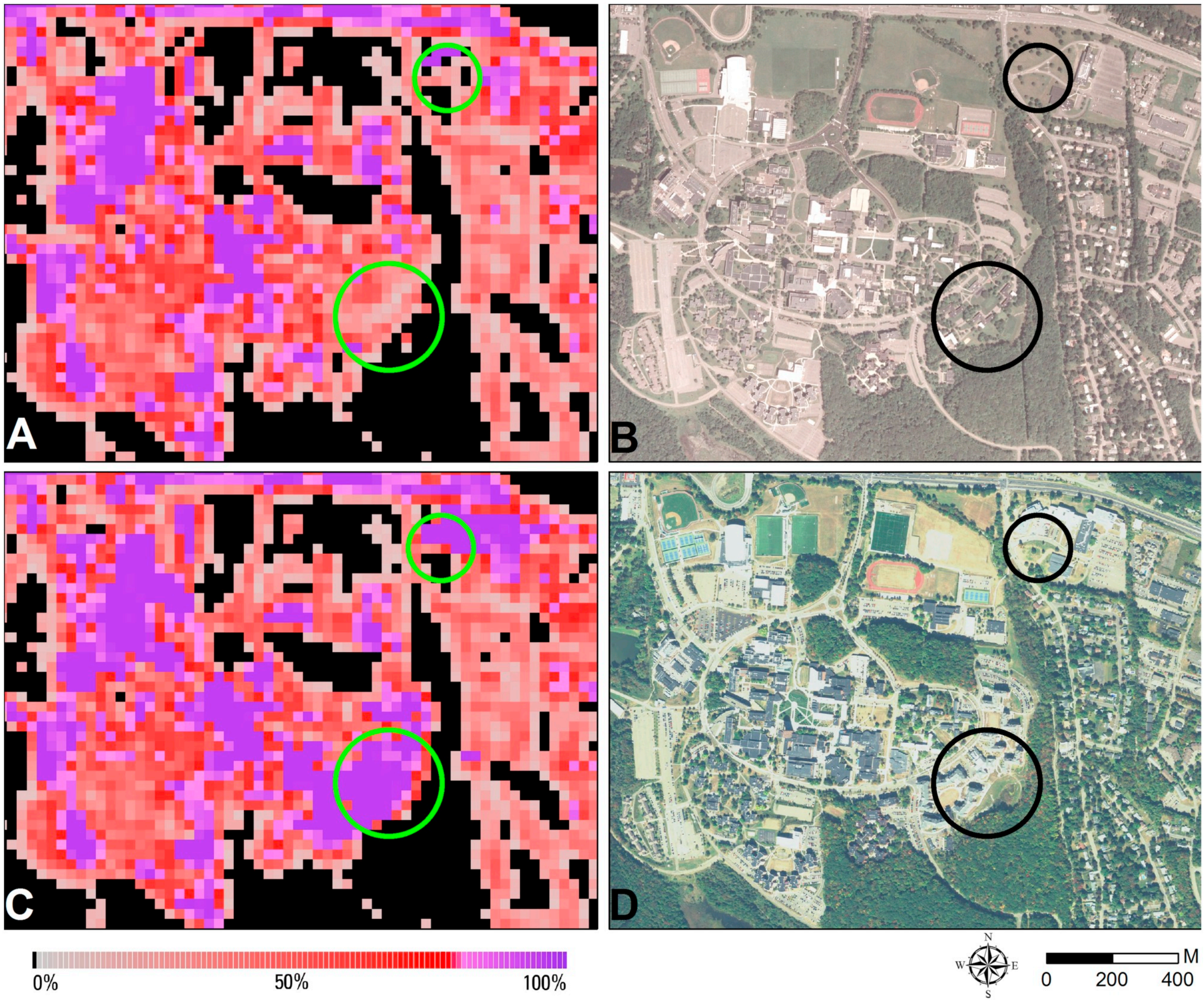

Fig. 12. Percent impervious surface increase at SUNY-Binghamton: (A) 2006 CSM-modeled percent impervious surface; (B) 2006 NAIP orthophoto; (C) 2014 CSM-modeled percent impervious surface; and (D) 2014 NAIP orthophoto.

bands (except the thermal band), and model with these four variables in the four VIR bands.

Scatterplots in Fig. 6 illustrates the modeled fraction against reference fraction. The performance of all random forest models is satisfactory, all of which have a slope higher than 0.87, an intercept less than or close to 3%, and an R-squared greater than 0.94. Comparatively, the 2011 NLCD percent impervious surface product only has a slope of 0.69, and an R-squared of 0.74 (Fig. 6E). Three accuracy metrics, RMSE, MAE, and SE, were calculated for these four random forest models with different combinations of bands and variables (see Table 1). Consistent with the findings of scatterplots, satisfactory performance of the four CSM models can be reached as well, as supported by high estimation precisions (with an RMSE of 7.5% and an MAE of 4.6%) and small bias (with an SE of 0.3%). Some interesting findings can be observed. First, CSM models with four variables per band (Fig. 6B, C and D) slightly outperform the CSM with all eight variables per band. Second, when using four variables per band, the CSM model that excludes the thermal band is slightly better than that using all bands. This is probably caused by the different spatial resolution of the thermal band and optical band, as well as the changing resolution of the thermal band itself in Landsat (120 m for Landsat 5, 60 m for Landsat 7, and 100 m for Landsat 8). Third, among CSM models with four variables per band, the model with all optical bands and the model with VIR bands are comparable with each other, and both are slightly higher than the other CSM models and NLCD product. While NLCD percent impervious surface has the best performance in low density developed area, the underestimation in high density developed area substantially affects the overall accuracy. In case that CSM is applied to a larger scale, Landsat bands of SWIR 1 and 2 may include useful information in other regions with different climates and environment settings. Therefore, we selected the CSM model in Fig. 6C using all optical bands (including Landsat bands 1 to 5 and 7) with four variables per band (a total of 24 variables) as the optimal CSM model for mapping fractional impervious surface based on the following results.

4.2. CSM for urban impervious surface fraction at one point in time

The resultant 2011 subpixel impervious surface of the entire Broome County estimated by CSM is shown in Fig. 7A. For comparison purposes, Fig. 7B, C, and D show the NAIP aerial photograph, NLCD percent impervious surface, and NLCD land cover classification product, respectively. The overall pattern of the CSM estimated subpixel impervious surface in Fig. 7A is similar to that of the three reference datasets. Impervious surfaces are mostly clustered within Triple Cities Area, and local transportation networks and fragmented residential areas can be visually observed outside the core city. No apparent

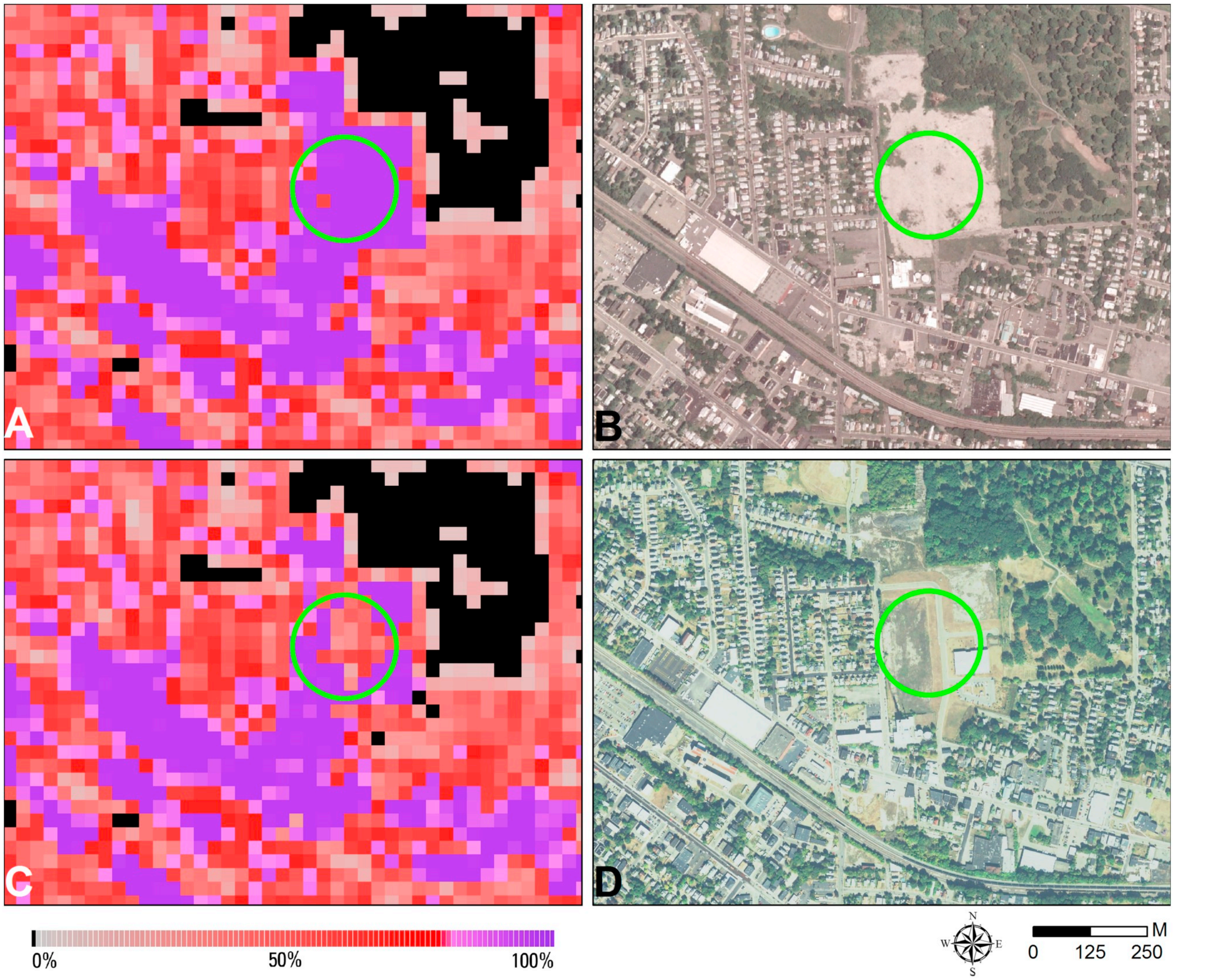

Fig. 13. Percent impervious surface decrease in West Side, Binghamton: (A) 2006 CSM-modeled percent impervious surface; (B) 2006 NAIP orthophoto; (C) 2014 CSM-modeled percent impervious surface; and (D) 2014 NAIP orthophoto.

underestimation or overestimation is found. We further zoom into low and high density developed areas and illustrate them in Figs. 8 and 9, respectively. Areas with low percent impervious surface are generally found in suburban and rural areas of the study area, such as scattered small settlements and local roads. Although such land covers located in urban fringes have long been challenges in urban mapping due to their small-scale and fragmented nature (Schneider et al., 2010), they can be precisely mapped using CSM as displayed in Fig. 8A. It is worth noting that, unlike NLCD percent imperviousness product, no ancillary data is used with the CSM model to assist in subpixel mapping of local roads and small settlements, but high precision and small bias comparable to those of NLCD product are associated with CSM (with an RMSE of 5.3% and an MAE of 3%) (see Table 1). Comparatively, small settlements are almost neglected in NLCD percent impervious surface data, which cannot be observed in Fig. 8C and D. Areas with high percent impervious surface (which are displayed as purple pixels in Figs. 7A, 8A, and 9A) can be found in the downtown Binghamton and its adjacent city centers, such as Oakdale mall in Johnson City, downtown Endicott, and Townsquare mall as well as SUNY-Binghamton campus in Vestal. As shown in Fig. 9A, high percent impervious surfaces cluster in downtown Binghamton (right in Fig. 9A), and along with main street in Johnson City and Westside Binghamton (upper left and upper center in Fig. 9A). Table 1 shows that CSM improves not only underestimation in high density developed areas (from an SE of −8% with NLCD to −3% with CSM), but also precision (with an RMSE of 10.7 and an MAE of 8.6%), comparing with NLCD percent imperviousness product (with an RMSE of 19% and an MAE of 13%). All these analyses suggest that better subpixel estimation results can be achieved by applying CSM, as it consistently outperforms the NLCD percent impervious surface product.

4.3. CSM for percent change of urban impervious surface between different years

Prior to illustrate the percent impervious surface change results, we need to find out the optimal threshold to exclude urban surface modification from urban impervious surface change. To this end, a sensitivity analysis was performed following (Wickham et al., 2013). Fig. 10 illustrates the impact of the thresholding on the change detection accuracy, where change is identified only if the impervious surface area changed (excluding surface modification). As the NDVI abrupt change threshold increases from 0 to 0.5 with an increment of 0.05, the user's accuracy rises and the producer's accuracy drops. The optimal threshold can be found at the intersection of the two curves at approximately 0.1 (i.e., the balance between omission and commission errors), which is then used as the cut-off point to reduce the impact of surface

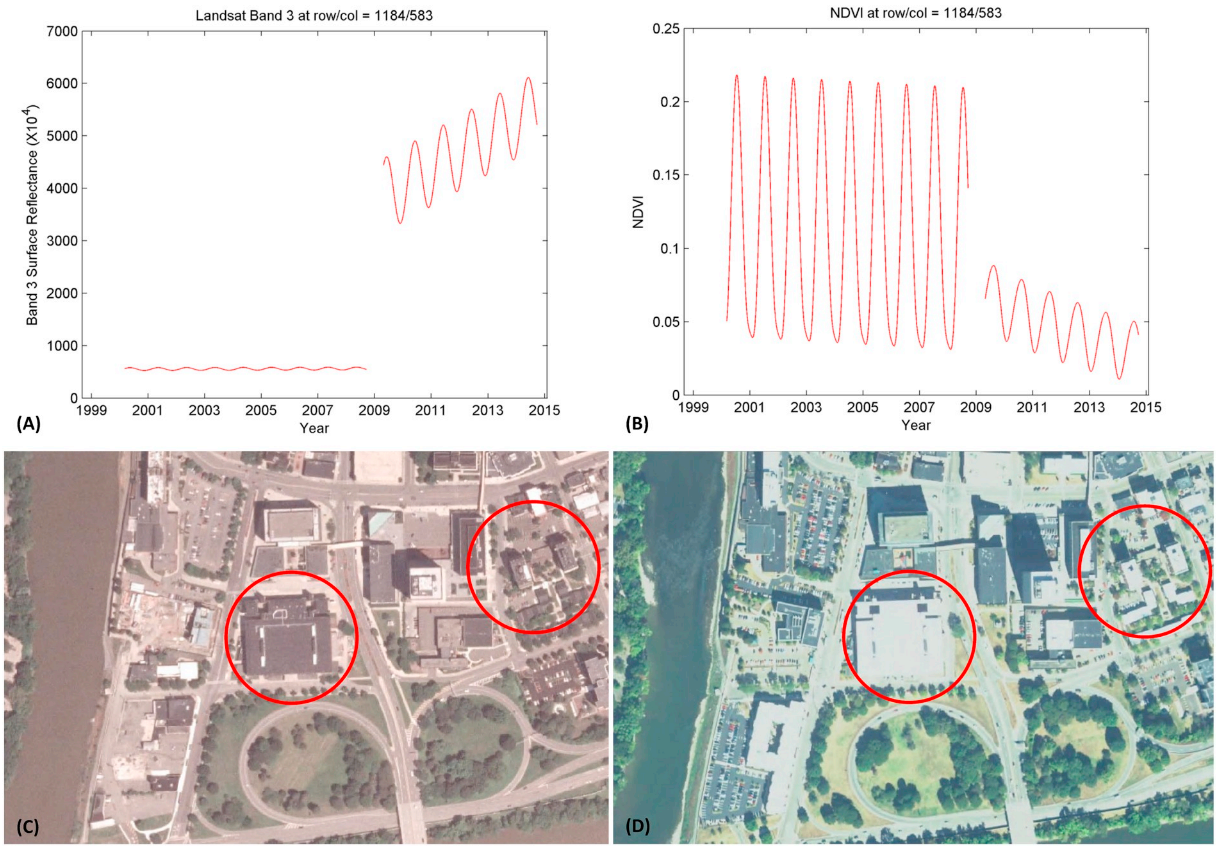

Fig. 14. (A) Detected land surface change shown as different kinds of time series models in Landsat band 3; (B) relatively small difference of overall NDVI between two time periods; (C) and (D) New concrete coatings on building roofs in downtown Binghamton (before and after).

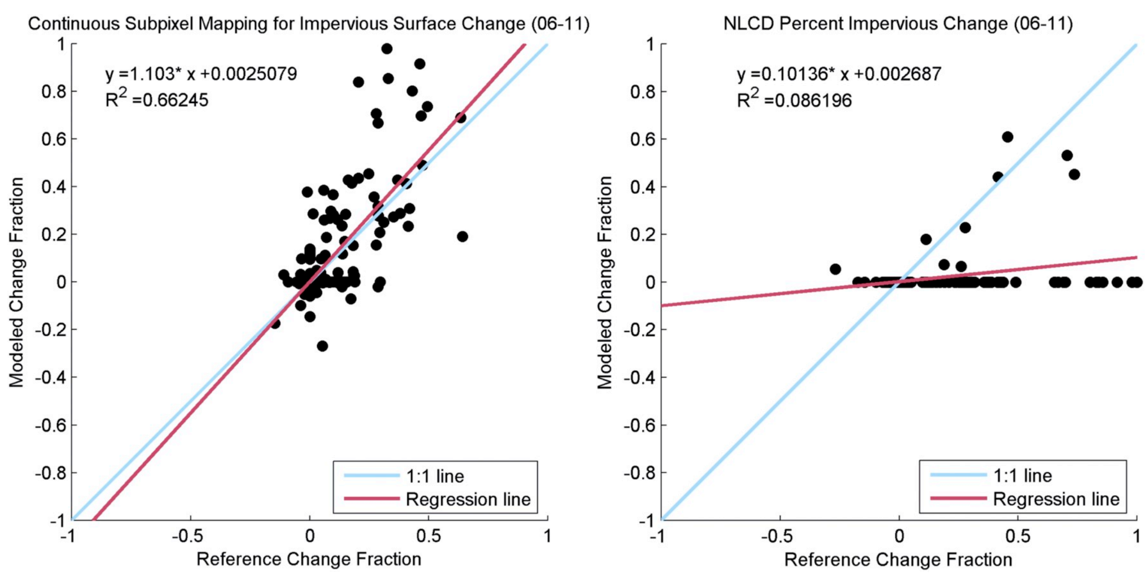

Fig. 15. Scatterplot between modeled and reference percent change of urban impervious surface using CSM, and scatterplot of NLCD percent impervious change between 2006 and 2011. (For interpretation of the references to color, the reader is referred to the web version of this article.)

modification.

In addition to deriving subpixel land cover at one point in time, CSM can be used to yield the fractional land cover change between any two timestamps. We further examined (both qualitatively and quantitatively) the impervious surface changes overtime on several typical sites in Binghamton. Fig. 11 illustrates the complete annual percent impervious surface change process on the campus of SUNY-Binghamton between 2000 and 2014. The blue and green boxes highlight the expansion and intensification with subpixel impervious surface increase in 2004 and 2011, respectively. Fig. 12 displays more details of campus developments. During the study period, SUNY-Binghamton decided to build more modern dormitories to accommodate its increasing undergraduate enrollments. In 2006, old dormitories, as well as the surrounding lawns, can be found in the Dickinson community in the lower circle in Fig. 12A and B. In 2014, the redevelopment finished (part of the community was open in 2011), and the campus landscape changes

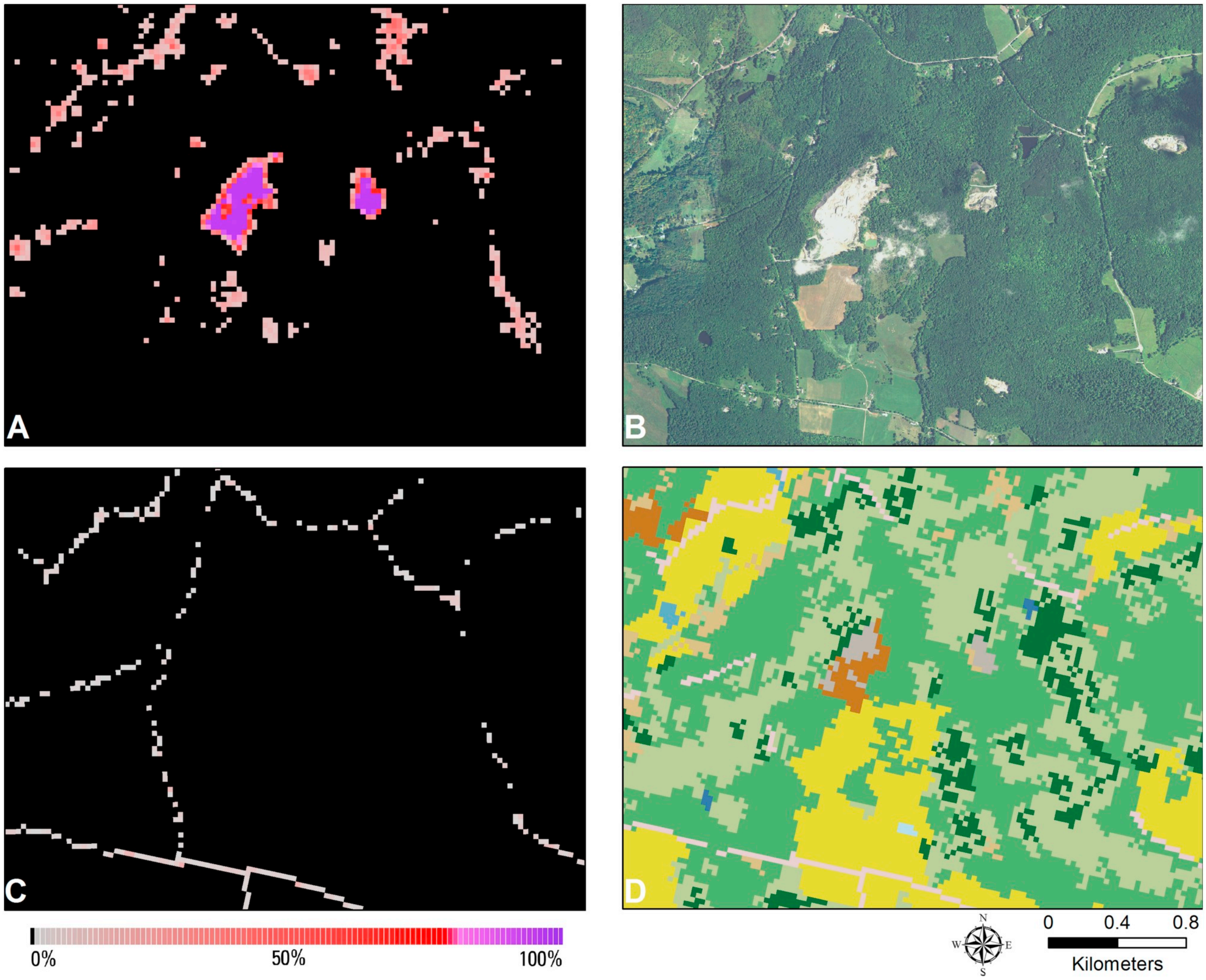

Fig. 16. An example of overestimation of percent impervious surface caused by bare soil in a mining site, (A) CSM result in 2011; (B) 2011 aerial photograph; (C) 2011 NLCD percent impervious surface; and (D) 2011 NLCD land cover classification.

Table 1
Accuracy comparison of CSM models with different band and variable combinations and the 2011 NLCD percent developed imperviousness product (the best accuracy metrics are shaded).

Band and time series model coefficient combinations	Overall areas			Low density developed areas			High density developed areas		
	RMSE (%)	MAE (%)	SE (%)	RMSE (%)	MAE (%)	SE (%)	RMSE (%)	MAE (%)	SE (%)
All bands (8 variables per band)	7.687	4.955	0.392	5.231	3.133	1.976	11.695	9.418	−3.486
All bands (4 variables per band)	7.371	4.687	0.216	5.043	2.913	1.726	11.183	9.031	−3.483
All optical bands (4 variables per band)	7.324	4.642	0.430	5.352	3.019	1.894	10.716	8.615	−3.153
VIR bands (4 variables per band)	7.411	4.603	0.196	5.193	2.866	1.767	11.108	8.854	−3.661
2011 NLCD ISA%	10.715	4.743	−3.534	3.781	1.773	−1.438	18.998	13.015	−8.667

include the transformation of trees to parking lots, and the demolition of old dormitories, as well as the most recent constructions of new and modern dormitories, which are shown in Fig. 12C and D. Later, the university also built a new facility, the Innovative Technologies Complex (ITC), as its new Engineering and Science Building. Located close to the main campus, the ITC facility also experienced significant land cover changes during the construction process. As shown in the upper circle in Fig. 12, the land used to be a large lawn in 2006 (see Fig. 12B), and grasses were completely removed and taken place by buildings and parking lots in 2014 (see Fig. 12D). The increases of impervious surface in magnitude on campus are appropriately characterized by using CSM. Another important and revolutionizing feature of CSM result is that, for pixels with no land surface change detected by CCDC, the estimated percent urban impervious surface remains relatively stable in different years. This is because they are estimated based on time series model coefficients which are consistent in time, rather than based on the reflectance of each Landsat image. Therefore, CSM will not suffer from the compounded errors from the post-classification comparison in detecting urban impervious change.

Comparatively, another form of urban transition, urban demolition and redevelopment, can also be found by using CSM in our study area. Such an urban transformation pattern, however, has rarely attracted much attention. Fig. 13 shows a representative example of the decreasing urban impervious surface in First Ward, Binghamton. The land in the green circle in Fig. 12 has been left abandoned for nearly two decades. This site used to be occupied by the former Anitec Image Technology Corporation. The company was closed in December 1999, and shortly in February 2000, its manufacturing facilities and buildings were torn down. With most of the structures being demolished and debris being cleaned later as shown in Fig. 13B, grasses gradually regrow on this site, which can be observed in Fig. 13D. Such a decrease of urban impervious surface that changed from an industrial site to natural grassland can be captured in the fraction cube as shown in both Figs. 13A (2006) and C (2014).

Except for urban intensification/expansion and urban demolition/redevelopment, urban surface modifications due to urban renewal can be detected by CSM as well. This type of urban transformations may not involve impervious surface change, and during this process, the function (or land use types) might or might not change. Examples include renovation from industrial use to residential use due to gentrification, or simply, building maintenance and new painting. Fig. 14 illustrates an example of modification in downtown Binghamton. In 2006, asphaltic roofs were discerned on several buildings, including an arena (the left circle), a few apartments, and office buildings (the right circle). However, it appears that the roofs of these buildings have been coating concrete as shown in 2014. Only with roof repair and preservation, such surface modifications should not be considered as the impervious surface change (increase or decrease). These modifications can be detected and filtered by the refinement processing in CSM, as shown in Fig. 14.

Quantitative analyses are also performed to measure the percent change. A scatterplot was derived by plotting the reference percent change of impervious surface by manual digitizing against the modeled change between 2006 and 2011 with CSM. It can be discerned in Fig. 15A that most of the plots cluster along the blue 1:1 line, indicating that most fractional changes are well estimated. The regression model of these plots has a slope of 1.1 and an intercept of 0.003, which also suggests a satisfactory percent change. It is worth noting that, not only positive change (e.g., the increase of fractional impervious surface) but also negative change (e.g., the decrease of percent impervious surface) are illustrated in Fig. 14A. For comparison purposes, we also created a scatterplot of NLCD percent imperviousness change (2006–2011) by using our manually digitized reference fraction data. Fig. 15B shows that the NLCD percent change data does not match reference percent change of impervious surface well. A large number of plots deviate from the 1:1 reference line and most of the changes are not detected in the NLCD percent imperviousness change. It is due primarily to the omission error of the impervious surface change in the NLCD product (Wickham et al., 2013), and the producer's accuracy of NLCD percent imperious surface change is found as low as 8%. In particular, the decrease of impervious surface is not taken into consideration in the NLCD percent change product (Wickham et al., 2013), which does not reflect all types of urban transitions. Accuracy metrics of precision and bias in Table 2 also support the considerable improvement with CSM. Almost all accuracy indicators are substantially improved from the NLCD percent change product, regardless of gain or loss of percent urban impervious surface.

5. Discussions

5.1. Comparisons with other subpixel mapping methods

One of the advantages of CSM is that it can yield a time series fraction cube (as shown in Fig. 11) with high accuracy for mapping fractional urban land cover at one point in time, as well as for detecting percent change in any time interval. The accuracy metrics using CSM in this research are comparable to, and even better than, those of previous studies. For example, by relating widely used vegetation indices (NDVI and SAVI) to percent impervious surface in various European cities, an RMSE of 14% and an R-squared of 0.77 are achieved in Kaspersen et al. (2015). Another example is the generation of annual percent impervious surface in Jakarta, Indonesia with an RMSE of 20% and an R-squared of 0.55 (Tsutsumida et al., 2016). In particular, by using the same machine learning method in the same study area, the best RMSE, MAE and SE are achieved at 9%, 6% and 3% respectively, as reported in Deng et al. (2017). Compared to CSM, the only difference is the data input with single-date or seasonal combination of Landsat images in their work. As such, the better performance of CSM is probably due to the temporal features extracted from time series model which can hardly be derived from a single-date image or even seasonal combinations.

In addition, percent urban impervious surface in low density developed areas can be characterized accurately in urban fringe areas by CSM. A noticeable example is that isolated and small human settlements in peri-urban areas are very difficult to detect. They are usually mapped in summer satellite images which are carefully selected (Schneider, 2012), or rely heavily on ancillary datasets (Homer et al., 2004; Yang et al., 2003b). For example, NLCD percent impervious surface product employs population density and DMSP nighttime light data to create an urban mask, and transportation network vector data was buffered and rasterized to generate a mask of local roads. Only pixels located within these masks are retained as urban pixels, otherwise, they are assumed to be rural lands with no impervious surface (Yang et al., 2003a). Small settlements outside the these masks are likely to be omitted due to its coarse resolution and low sensor sensitivity of nighttime light data, as relatively large omission error is reported in the literature (Wickham et al., 2013). This results in severe underestimation in suburban and rural areas in the NLCD products. By using CSM, temporal information is reflected by the coefficients and model fits of time series models, which does not require visual examination, careful manual selection of appropriate satellite images, or excessive ancillary data. It needs to be very cautious when using these ancillary data sets, especially for subpixel urban land cover mapping and change detection. However, it should be noted that NLCD has been

Table 2
Accuracy comparison of percent change of impervious surface using CSM and 2006 to 2011 NLCD Percent Developed Imperviousness Change product.

	%Change in overall areas			%Change in low density developed areas			%Change in high density developed areas		
	RMSE (%)	MAE (%)	SE (%)	RMSE (%)	MAE (%)	SE (%)	RMSE (%)	MAE (%)	SE (%)
CSM	14.387	8.639	−1.346	9.485	6.162	1.984	22.476	15.848	−10.011
NLCD ISA%	25.519	15.548	−10.304	13.732	4.764	−4.762	59.694	53.413	−52.032

successfully applied to the CONUS in past two decades, and it is not surprising that the accuracy in a middle-size city may be slightly lower than its average level, as they may not have sufficient training samples in this area. In addition to bringing more temporal information, the time series model smooths out the noise in the images, especially high "signal to noise" ratio may be found in those low density developed areas.

5.2. Transferable random forest model in different timestamps

With CSM, training samples were only obtained from one point in time (digitizing on an aerial photograph) and employed to train the random forest model for the Landsat time series to derive the time series fraction cube. The achieved high estimation accuracy proves the effectiveness of the transferable random forest model. This is due mainly to the fact that the input variables in random forest are not image reflectance as traditional studies, but are the coefficients and model fits of the time series models. Even when land cover changes occur, time series models of the new land cover type remain similar to those of the same type which are obtained from the acquisition time of training samples. As various types of land covers have been included in training samples, the trained random forest model, therefore, is transferable to and works well for any other timestamp. Obtaining training data of fractional land covers is a labor-intensive task. In traditional studies, they are usually derived by manual digitizing or classification on high-resolution images. One approach is to obtain training samples multiple times in different year separately. Another way is to take advantage of invariant historical training samples on other images. That is, all historical samples need to be carefully examined to assure that no land cover changed between the high-resolution data and Landsat image, and any changed samples are excluded from the sample pool (Li et al., 2015; Xian and Crane, 2005; Yang et al., 2003b). New prediction models need to be built on every Landsat image taken on different acquisition dates. Not only is the processing very time consuming (a large number of images in the time series), but also it is associated with compound errors and is not suitable for change detection (Zhu, 2017). Both the accuracy and efficiency have been much improved by using the transferable random forest model for the continuous mapping of subpixel fractional land covers at different acquisition time.

5.3. Identification of different patterns of urban transformation

The CSM algorithm can automatically and accurately reflect the status of different patterns of urban transitions. The resultant fraction cube from CSM records the entire urban transformation process. It provides a complete document of urban development for government and local planning department, including the change magnitude of fractional land cover and time of land cover change. With these spatial and temporal details, the status of urban transitions can be identified, including urban expansion/intensification (growth of impervious surface), urban demolition/redevelopment (loss of impervious surface), as well as surface modification (new painting or coating for maintenance purposes while no impervious change occurs). These different patterns of urban transitions have rarely been reported or adequately characterized in the literature. Most existing studies built on an assumption that once urban is developed, irreversible process (i.e., from urban to natural lands) cannot take place (Song et al., 2016). Although this assumption may be valid for a relatively long period, urban land covers are not always static all the time. The assumption of irreversible urban development does not work in a shrinking city, for example in our study area, as well as in the large Rust Belt region in the United States where there are a large number of brownfield or abandoned house demolitions and redevelopment programs. Comparatively, due to the data-driven nature of CSM, no empirical assumption is required, and any types of urban transitions can be characterized accurately with subpixel urban impervious surface using Landsat time series in an automated manner. In particular, the identification of urban surface modification and its differentiation from other urban transitions have rarely been done in the literature.

5.4. Continuous monitoring of urban dynamics

CSM allows continuous (both spatially and temporally) monitoring of urban transitions at the subpixel level, which has rarely been implemented in the literature. As soon as the latest Landsat or Landsat-like images are available for a study area, they can be loaded to the collected long-term observations. With such a mechanism, continuous monitoring and detection of the most recent subpixel land cover changes in urban areas can be implemented. The use of all clear observations with Landsat time series not only increases mapping efficiency by simplifying some preprocessing steps, but also substantially improves the accuracy of change detection. Preprocessing steps in the literature, such as careful selection of a completely cloud-free image, and generation of a cloud-free mosaic, are not required in the proposed algorithm. Both traditional methods require the use of all images taken for a specific year based on several predefined criteria, which are collected at the end of that year. These methods always result in a delay in time, and cannot generate the most recent urban mapping which is always of great necessity, especially in the fast-developing area. Comparatively, the use of CSM can provide the latest subpixel urban land cover dynamic information to researchers, social scientists, and policymakers for various applied practices.

5.5. Limitations and future works

Other than the aforementioned advantages, CSM has its own limitations. First, despite the aforementioned improvements, CSM does not entirely solve the confusions between spectrally similar land covers and urban impervious surface, resulting in the overestimation of percent impervious surface in rural and suburban areas. In our study area, overestimations are primarily attributed to the similar spectral-temporal feature between urban impervious surface and some temporally consistent barren lands (similar to commission errors in classification). Fig. 16 illustrates an example of overestimation of percent urban impervious surface in a bare soil pixel in a mining site. To reduce this type of overestimations/commission errors, the easiest approach is to collect more training data of the temporally consistent pixels with low percentage of urban impervious surface, as those are the pixels where CSM struggles. We can also add a preprocessing step in the future to filter those spectrally similar pixels. This may be done by using more training samples for barren and urban pixels, followed by the data-driven determination with CCDC land cover classification to decide the type of a pixel. If it is determined as an urban pixel, we can use the CMS approach to estimate its fraction of urban impervious surface. With such an additional step in CCDC, we anticipate that most of the commission errors will be substantially removed. In terms of omission errors, we hardly found any omission error of urban imperviousness change in our study area. Omission error of changed pixels using CCDC can be achieved as low as 2.3% (Zhu and Woodcock, 2014a). The high sensitivity on urban change detection has also been proved in our research, by which even urban surface modification can be identified. Based on its high accuracy and high sensitivity, omission errors are not severe for mapping subpixel urban change in our study area. Second, since the input variables are based on time series models from dense time clear observations, this method is computationally expensive and requires large data storage. This problem needs to be better addressed, particularly for mapping percent land cover dynamics in a larger area in a longer period. More experiments in future studies are warranted to further improve the proposed CSM algorithm to accommodate these limitations, and to make this algorithm more adaptive to different environments before it becomes operational for mapping large areas. In the future, we will also explore the inclusion of the spatial domain of

Landsat data to better identify urban extent and to separate the similar land covers.

6. Conclusions

We developed a new method called CSM for mapping and updating urban impervious surface at the subpixel level using Landsat time series. We first estimated time series models for each pixel and each spectral band based on all clear observations in the past fifteen years, and the time series models are used to detect any land surface change. Later, the coefficients of the time series models and RMSEs from model fit were then employed as the inputs of random forest regressor. To better construct random forest regression models, we analyzed variable importance and tested different combinations of variables, and recommend constructing models based on four variables per band using all six optical bands (i.e., a total of 24 variables). We have successfully applied this algorithm to map subpixel urban impervious surface and characterize its dynamic in Broome County, New York.

Based on the results and analyses, we made a few conclusions as follows. First, CSM can provide subpixel urban impervious surface maps seamlessly at any point in time by integrating subpixel mapping and time series analysis. Second, CSM can derive subpixel urban impervious surface change between any time interval with high accuracy, by which sub-annual percent urban impervious surface change products can be easily generated. The accuracy of percent impervious surface change is much higher than that of the 2006 to 2011 NLCD percent developed imperviousness product. Third, this approach can detect not only urban expansion/intensification (percent urban impervious surface gain), but also different patterns of urban transitions overtime, such as urban demolition/redevelopment (percent urban impervious surface loss), and urban surface modifications (unchanged percent urban impervious surface due to no mechanical change). Finally, CSM works well in one of the cloudiest regions in the CONUS. With the unique characteristics of the CSM algorithm, we believe that, in addition to urban impervious surface, CSM has the potential to map and monitor other land cover types (e.g., tree canopy, and shrublands) in a reliable and efficient way at the subpixel level and large scales.

Acknowledgement

The authors would like to thank the anonymous reviewers, the Editor-in-Chief and Guest Editors for their constructive comments and suggestions.

Appendix A. Appendix

Appendix Fig. 1 shows the redevelopment at MacArthur Elementary School located in Southside, Binghamton. With less than two hundred meters from the Susquehanna River, this elementary school was destroyed by two flooding events in 2009 and 2011 due to Tropical Storm Lee and Hurricane Irene. It was demolished in October 2013, and rebuilt on a raised site with a risk-conscious design. The school reconstruction is apparent when comparing the resultant percent urban impervious surface between 2006 (Appendix Fig. 1A) and 2014 (Appendix Fig. 1C). The increase of percent impervious surface can be found not only in the south but also in the north in this study area. Appendix Fig. 2 illustrates the growth of percent urban impervious surface near Chenango Bridge in north Binghamton, due to the requirement of storage space from Broome County highway division. During 2006 and 2014, trees and grasslands were cleared and transformed into concrete pavement for industrial storage use, as shown in Appendix Fig. 2A and C. Overall, these examples of urban redevelopment and expansion with increasing percent impervious surface can be effectively highlighted, and for areas that have not changed, percent change of urban impervious surface is hardly observed.

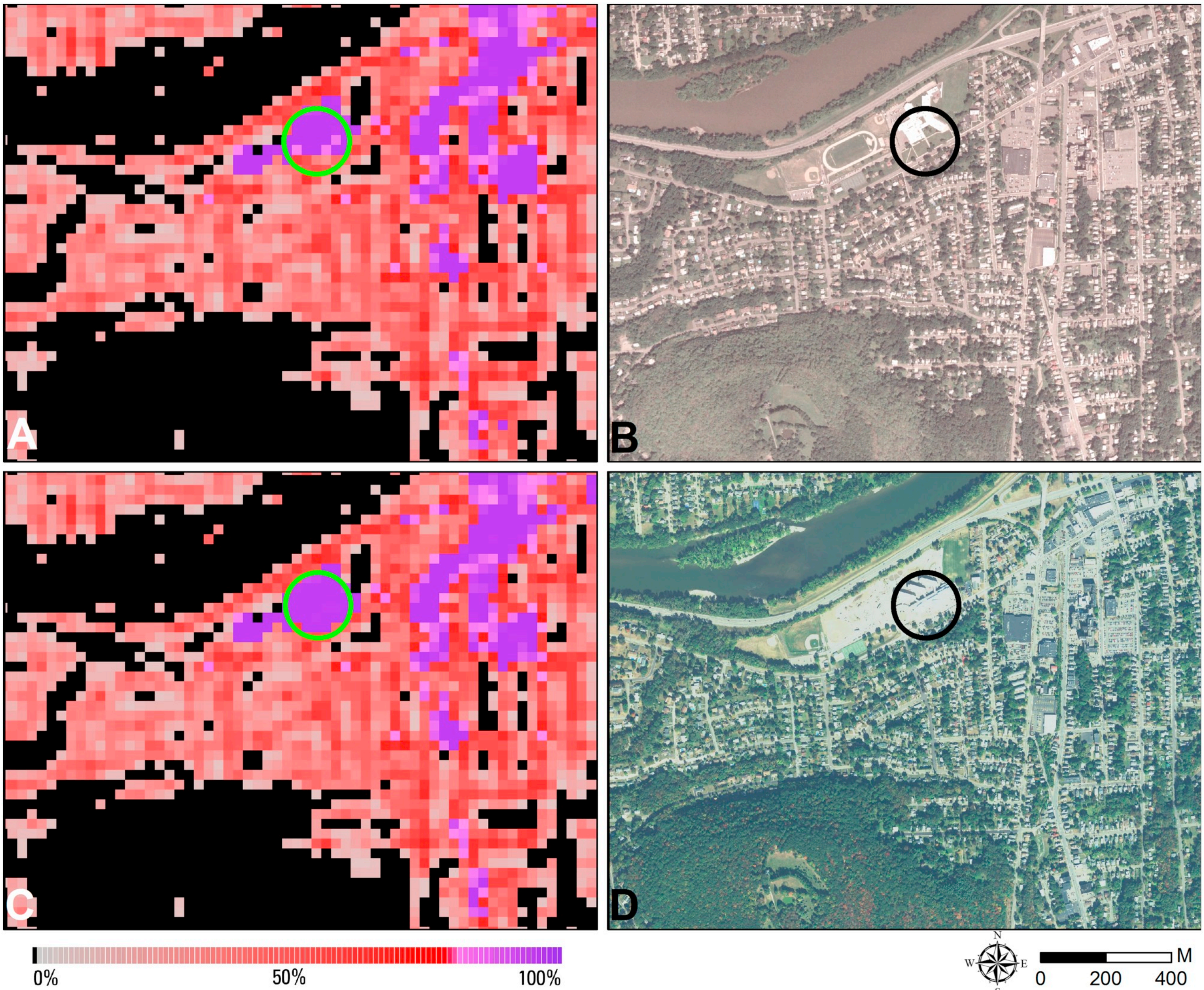

Appendix Fig. 1. Percent impervious surface increase in Southside, Binghamton: (A) 2006 CSM-modeled percent impervious surface; (B) 2006 NAIP orthophoto; (C) 2014 CSM-modeled percent impervious surface; and (D) 2014 NAIP orthophoto

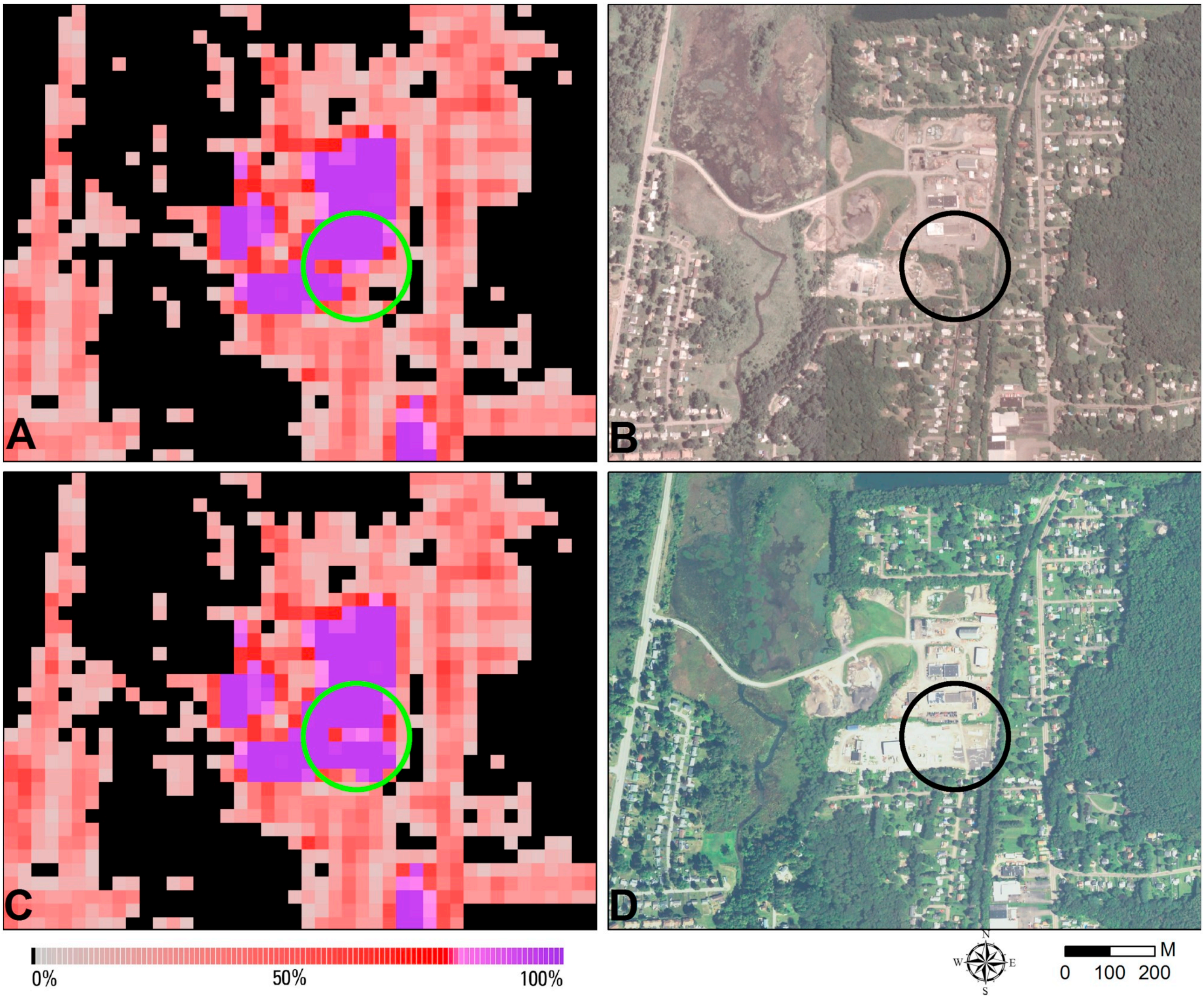

Appendix Fig. 2. Percent impervious surface increase in North Binghamton: (A) 2006 CSM-modeled percent impervious surface; (B) 2006 NAIP orthophoto; (C) 2014 CSM-modeled percent impervious surface; and (D) 2014 NAIP orthophoto

References

Adams, J.B., Smith, M.O., Johnson, P.E., 1986. Spectral mixture modeling: a new analysis of rock and soil types at the Viking lander 1 site. J. Geophys. Res. 91, 8098–8112. https://doi.org/10.1029/JB091iB08p08098.

Arnold, C.L., Gibbons, C.J., 1996. Impervious surface coverage: the emergence of a key environmental indicator. J. Am. Plan. Assoc. 62, 243–258. https://doi.org/10.1080/01944369608975688.

Brabec, E., Schulte, S., Richards, P.L., 2002. Impervious surfaces and water quality: a review of current literature and its implications for watershed planning. J. Plan. Lit. https://doi.org/10.1177/088541202400903563.

Breiman, L., 2001. Random forests. Mach. Learn. 45, 5–32. https://doi.org/10.1023/A:1010933404324.

Brooks, E.B., Wynne, R.H., Thomas, V.A., Blinn, C.E., Coulston, J.W., 2014. On-the-fly massively multitemporal change detection using statistical quality control charts and landsat data. IEEE Trans. Geosci. Remote Sens. 52, 3316–3332. https://doi.org/10.1109/TGRS.2013.2272545.

Center for Watershed Protection, 2003. Impacts of impervious cover on aquatic systems. Watershed Prot. Res. Monogr. 1–142.

Chabaeva, A., Civco, D.L., Hurd, J.D., 2009. Assessment of impervious surface estimation techniques. J. Hydrol. Eng. 14, 377–387. https://doi.org/10.1061/(ASCE)1084-0699(2009)14:4(377).

Cohen, B., 2004. Urban growth in developing countries: a review of current trends and a caution regarding existing forecasts. World Dev. 32, 23–51. https://doi.org/10.1016/j.worlddev.2003.04.008.

Cohen, W.B., Yang, Z., Kennedy, R., 2010. Detecting trends in forest disturbance and recovery using yearly Landsat time series: 2. TimeSync - tools for calibration and validation. Remote Sens. Environ. 114, 2911–2924. https://doi.org/10.1016/j.rse.2010.07.010.

Coulston, J.W., Moisen, G.G., Wilson, B.T., Finco, M.V., Cohen, W.B., Brewer, C.K., 2012. Modeling percent tree canopy cover: a pilot study. Photogramm. Eng. Remote. Sens. 78, 715–727.

Coulston, J.W., Jacobs, D.M., King, C.R., Elmore, I.C., 2013. The influence of multi-season imagery on models of canopy cover: a case study. Photogramm. Eng. Remote. Sens. 37919, 469–477.

Deng, C., 2016. Automated construction of multiple regional libraries for neighborhoodwise local multiple endmember unmixing. IEEE J. Sel. Top. Appl. Earth Obs. Remote Sens. 9. https://doi.org/10.1109/JSTARS.2016.2541660.

Deng, C., Ma, J., 2015. Viewing urban decay from the sky: a multi-scale analysis of residential vacancy in a shrinking U.S. city. Landsc. Urban Plan. 141. https://doi.org/10.1016/j.landurbplan.2015.05.002.

Deng, C., Wu, C., 2013. A spatially adaptive spectral mixture analysis for mapping subpixel urban impervious surface distribution. Remote Sens. Environ. 133, 62–70. https://doi.org/10.1016/j.rse.2013.02.005.

Deng, C., Wu, C., 2013a. Examining the impacts of urban biophysical compositions on surface urban heat island: a spectral unmixing and thermal mixing approach. Remote Sens. Environ. 131. https://doi.org/10.1016/j.rse.2012.12.020.

Deng, C., Wu, C., 2013c. The use of single-date MODIS imagery for estimating large-scale urban impervious surface fraction with spectral mixture analysis and machine learning techniques. ISPRS J. Photogramm. Remote Sens. 86. https://doi.org/10.1016/j.isprsjprs.2013.09.010.

Deng, C., Li, C., Zhu, Z., Lin, W., Xi, L., 2017. Subpixel urban impervious surface mapping: the impact of input Landsat images. ISPRS J. Photogramm. Remote Sens. 133, 89–103. https://doi.org/10.1016/j.isprsjprs.2017.09.015.

Friedman, J., Hastie, T., Tibshirani, R., 2008. Sparse inverse covariance estimation with the graphical lasso. Biostatistics 9 (3), 432–441.

Friedman, J., Hastie, T., Tibshirani, R., 2010. Regularization paths for generalized linear

models via coordinate descent. J. Stat. Softw. 33 (1), 1.
Gao, F., de Colstoun, E.B., Ma, R., Weng, Q., Masek, J.G., Chen, J., Pan, Y., Song, C., 2012. Mapping impervious surface expansion using medium-resolution satellite image time series: a case study in the Yangtze River Delta, China. Int. J. Remote Sens. 33, 7609–7628. https://doi.org/10.1080/01431161.2012.700424.
Hamunyela, E., Verbesselt, J., Herold, M., 2016. Using spatial context to improve early detection of deforestation from Landsat time series. Remote Sens. Environ. 172, 126–138. https://doi.org/10.1016/j.rse.2015.11.006.
Hansen, M.C., Defries, R., Townshend, J.R.G., Sohlberg, R., 2000. Global land cover classification at 1 km spatial resolution using a classification tree approach. Int. J. Remote Sens. 21, 1331–1364. https://doi.org/10.1080/014311600210209.
Hansen, M.C., Krylov, A., Tyukavina, A., Potapov, P.V., Turubanova, S., Zutta, B., Ifo, S., Margono, B., Stolle, F., Moore, R., 2016. Humid tropical forest disturbance alerts using Landsat data. Environ. Res. Lett. 11, 034008. https://doi.org/10.1088/1748-9326/11/3/034008.
Homer, C., Huang, C., Yang, L., Wylie, B., Coan, M., 2004. Development of a 2001 national land-cover database for the United States. Photogramm. Eng. Remote. Sens. 70, 829–840. https://doi.org/10.14358/PERS.70.7.829.
Homer, C.G., Dewitz, J.A., Yang, L., Jin, S., Danielson, P., Xian, G., Coulston, J., Herold, N.D., Wickham, J.D., Megown, K., 2015. Completion of the 2011 National Land Cover Database for the conterminous United States-representing a decade of land cover change information. Photogramm. Eng. Remote. Sens. 81, 345–354. https://doi.org/10.14358/PERS.81.5.345.
Huang, C., Goward, S.N., Masek, J.G., Thomas, N., Zhu, Z., Vogelmann, J.E., 2010. An automated approach for reconstructing recent forest disturbance history using dense Landsat time series stacks. Remote Sens. Environ. 114, 183–198. https://doi.org/10.1016/j.rse.2009.08.017.
Kaspersen, P.S., Fensholt, R., Drews, M., 2015. Using Landsat vegetation indices to estimate impervious surface fractions for European cities. Remote Sens. 7, 8224–8249. https://doi.org/10.3390/rs70608224.
Li, X., Gong, P., Liang, L., 2015. A 30-year (1984–2013) record of annual urban dynamics of Beijing City derived from Landsat data. Remote Sens. Environ. 166, 78–90. https://doi.org/10.1016/j.rse.2015.06.007.
Li, L., Lu, D., Kuang, W., 2016. Examining urban impervious surface distribution and its dynamic change in Hangzhou metropolis. Remote Sens. 8, 19–24. https://doi.org/10.3390/rs8030265.
Masek, J.G., Huang, C., Wolfe, R., Cohen, W., Hall, F., Kutler, J., Nelson, P., 2008. North American forest disturbance mapped from a decadal Landsat record. Remote Sens. Environ. 112, 2914–2926. https://doi.org/10.1016/j.rse.2008.02.010.
Meyer, J.L., Paul, M.J., Taulbee, W.K., 2005. Stream ecosystem function in urbanizing landscapes stream ecosystem function in urbanizing landscapes. J. N. Am. Benthol. Soc. 24, 602–612. https://doi.org/10.1899/04-021.1.
Michishita, R., Jiang, Z., Xu, B., 2012. Monitoring two decades of urbanization in the Poyang Lake area, China through spectral unmixing. Remote Sens. Environ. 117, 3–18. https://doi.org/10.1016/j.rse.2011.06.021.
Nash, D.B., Conel, J.E., 1974. Spectral reflectance systematics for mixtures of powdered hypersthene, labradorite, and ilmenite. J. Geophys. Res. 79, 1615–1621. https://doi.org/10.1029/JB079i011p01615.
Paul, M.J., Meyer, J.L., 2001. Treams in the urban landscape. Annu. Rev. Ecol. Syst. 32, 333–365. https://doi.org/10.1146/annurev.ecolsys.32.081501.114040.
Potere, D., Schneider, A., 2007. A critical look at representations of urban areas in global maps. GeoJournal 69, 55–80. https://doi.org/10.1007/s10708-007-9102-z.
Powell, R.L., Roberts, D.A., Dennison, P.E., Hess, L.L., 2007. Sub-pixel mapping of urban land cover using multiple endmember spectral mixture analysis: Manaus, Brazil. Remote Sens. Environ. 106, 253–267. https://doi.org/10.1016/j.rse.2006.09.005.
Roberts, D.a., Gardner, M., Church, R., Ustin, S., Scheer, G., Green, R.O., 1998. Mapping chaparral in the santa monica mountains using multiple spectral mixture models. Remote Sens. Environ. 65, 267–279. https://doi.org/10.1016/S0034-4257(98)00037-6.
Schmidt, G., Jenkerson, C., Masek, J., Vermote, E., Gao, F., 2013. Landsat Ecosystem Disturbance Adaptive Processing System (LEDAPS) algorithm description. In: Open-file Rep. 2013-1057, pp. 1–27 (doi:No. 2013-1057).
Schneider, A., 2012. Monitoring land cover change in urban and peri-urban areas using dense time stacks of Landsat satellite data and a data mining approach. Remote Sens. Environ. 124, 689–704. https://doi.org/10.1016/j.rse.2012.06.006.
Schneider, A., Friedl, M.A., Potere, D., 2010. Mapping global urban areas using MODIS 500-m data: new methods and datasets based on “urban ecoregions”. Remote Sens. Environ. 114, 1733–1746. https://doi.org/10.1016/j.rse.2010.03.003.
Schueler, T.R., 1994. The importance of imperviousness. Watershed Prot. Tech. 1, 100–111.
Schueler, T.R., Fraley-McNeal, L., Cappiella, K., 2009. Is impervious cover still important? Review of recent research. J. Hydrol. Eng. 14, 309–315. https://doi.org/10.1061/(ASCE)1084-0699(2009)14:4(309).
Seto, K.C., 2009. Global urban issues: a primer. In: Global Mapping of Human Settlements: Experiences, Datasets, and Prospects, pp. 3–9.
Shahtahmassebi, A.R., Song, J., Zheng, Q., Blackburn, G.A., Wang, K., Huang, L.Y., Pan, Y., Moore, N., Shahtahmassebi, G., Sadrabadi Haghighi, R., Deng, J.S., 2016. Remote sensing of impervious surface growth: a framework for quantifying urban expansion and re-densification mechanisms. Int. J. Appl. Earth Obs. Geoinf. 46, 94–112. https://doi.org/10.1016/j.jag.2015.11.007.
Skougaard Kaspersen, P., Høegh Ravn, N., Arnbjerg-Nielsen, K., Madsen, H., Drews, M., 2017. Comparison of the impacts of urban development and climate change on exposing European cities to pluvial flooding. Hydrol. Earth Syst. Sci. 21, 4131–4147. https://doi.org/10.5194/hess-21-4131-2017.
Song, X.P., Sexton, J.O., Huang, C., Channan, S., Townshend, J.R., 2016. Characterizing the magnitude, timing and duration of urban growth from time series of Landsat-based estimates of impervious cover. Remote Sens. Environ. 175, 1–13. https://doi.org/10.1016/j.rse.2015.12.027.
Tsutsumida, N., Comber, A., Barrett, K., Saizen, I., Rustiadi, E., 2016. Sub-pixel classification of MODIS EVI for annual mappings of impervious surface areas. Remote Sens. 8. https://doi.org/10.3390/rs8020143.
UNDESA, 2018. World Urbanization Prospects: The 2018 Revision. (doi:(ST/ESA/SER.A/366)).
Vermote, E., Justice, C., Claverie, M., Franch, B., 2016. Preliminary analysis of the performance of the Landsat 8/OLI land surface reflectance product. Remote Sens. Environ. 185, 46–56. https://doi.org/10.1016/j.rse.2016.04.008.
Weng, Q., Lu, D., Schubring, J., 2004. Estimation of land surface temperature-vegetation abundance relationship for urban heat island studies. Remote Sens. Environ. 89, 467–483. https://doi.org/10.1016/j.rse.2003.11.005.
Wickham, J.D., Stehman, S.V., Gass, L., Dewitz, J., Fry, J.A., Wade, T.G., 2013. Accuracy assessment of NLCD 2006 land cover and impervious surface. Remote Sens. Environ. 130, 294–304. https://doi.org/10.1016/j.rse.2012.12.001.
Wu, C., 2004. Normalized spectral mixture analysis for monitoring urban composition using ETM+ imagery. Remote Sens. Environ. 93, 480–492. https://doi.org/10.1016/j.rse.2004.08.003.
Xiam, G., Homer, C., Dewitz, J., Fry, J., Hossain, N., Wickham, J., 2011. National land cover database 2006: percent impervious product. Pe&Rs 77, 754–762.
Xian, G., Crane, M., 2005. Assessments of urban growth in the Tampa Bay watershed using remote sensing data. Remote Sens. Environ. 97, 203–215. https://doi.org/10.1016/j.rse.2005.04.017.
Xian, G., Homer, C., 2010. Updating the 2001 national land cover database impervious surface products to 2006 using landsat imagery change detection methods. Remote Sens. Environ. 114, 1676–1686. https://doi.org/10.1016/j.rse.2010.02.018.
Xian, G., Homer, C., Meyer, D., Granneman, B., 2013. An approach for characterizing the distribution of shrubland ecosystem components as continuous fields as part of NLCD. ISPRS J. Photogramm. Remote Sens. 86, 136–149. https://doi.org/10.1016/j.isprsjprs.2013.09.009.
Xian, G., Homer, C., Rigge, M., Shi, H., Meyer, D., 2015. Characterization of shrubland ecosystem components as continuous fields in the Northwest United States. Remote Sens. Environ. 168, 286–300. https://doi.org/10.1016/j.rse.2015.07.014.
Yang, L., Huang, C., Homer, C.G., Wylie, B.K., Coan, M.J., 2003a. An approach for mapping large-area impervious surfaces: synergistic use of landsat 7 ETM+ and high resolution imagery. Can. J. Remote. Sens. 29, 230–240. https://doi.org/10.5589/m02-098.
Yang, L., Xian, G., Klaver, J.M., Deal, B., 2003b. Urban land-cover change detection through sub-pixel imperviousness mapping using remotely sensed data. Photogramm. Eng. Remote. Sens. 69, 1003–1010. https://doi.org/10.14358/PERS.69.9.1003.
Yuan, F., Bauer, M.E., 2007. Comparison of impervious surface area and normalized difference vegetation index as indicators of surface urban heat island effects in Landsat imagery. Remote Sens. Environ. 106, 375–386. https://doi.org/10.1016/j.rse.2006.09.003.
Zhu, Z., 2017. Change detection using landsat time series: a review of frequencies, preprocessing, algorithms, and applications. ISPRS J. Photogramm. Remote Sens. 130, 370–384. https://doi.org/10.1016/j.isprsjprs.2017.06.013.
Zhu, Z., Woodcock, C.E., 2012. Object-based cloud and cloud shadow detection in Landsat imagery. Remote Sens. Environ. 118, 83–94. https://doi.org/10.1016/j.rse.2011.10.028.
Zhu, Z., Woodcock, C.E., 2014a. Continuous change detection and classification of land cover using all available Landsat data. Remote Sens. Environ. 144, 152–171. https://doi.org/10.1016/j.rse.2014.01.011.
Zhu, Z., Woodcock, C.E., 2014b. Automated cloud, cloud shadow, and snow detection in multitemporal Landsat data: an algorithm designed specifically for monitoring land cover change. Remote Sens. Environ. 152, 217–234. https://doi.org/10.1016/j.rse.2014.06.012.
Zhu, Z., Wang, S., Woodcock, C.E., 2015a. Improvement and expansion of the Fmask algorithm: cloud, cloud shadow, and snow detection for Landsats 4–7, 8, and sentinel 2 images. Remote Sens. Environ. 159, 269–277. https://doi.org/10.1016/j.rse.2014.12.014.
Zhu, Z., Woodcock, C.E., Holden, C., Yang, Z., 2015b. Generating synthetic Landsat images based on all available Landsat data: predicting Landsat surface reflectance at any given time. Remote Sens. Environ. 162, 67–83. https://doi.org/10.1016/j.rse.2015.02.009.
Zhu, Z., Fu, Y., Woodcock, C.E., Olofsson, P., Vogelmann, J.E., Holden, C., Wang, M., Dai, S., Yu, Y., 2016. Including land cover change in analysis of greenness trends using all available Landsat 5, 7, and 8 images: a case study from Guangzhou, China (2000–2014). Remote Sens. Environ. 185, 243–257. https://doi.org/10.1016/j.rse.2016.03.036.